

# Optimization of the Neutrino Factory, revisited

October 22, 2018

SANJIB KUMAR AGARWALLA<sup>a</sup>, PATRICK HUBER<sup>b</sup>,  
JIAN TANG<sup>c</sup>, WALTER WINTER<sup>d</sup>

<sup>a</sup> *Instituto de Física Corpuscular, CSIC-Universitat de València,  
Apartado de Correos 22085, E-46071 Valencia, Spain*

<sup>a,b</sup> *Department of Physics, Virginia Tech, Blacksburg, VA24061, USA*

<sup>c,d</sup> *Institut für Theoretische Physik und Astrophysik, Universität Würzburg,  
D-97074 Würzburg, Germany*

## Abstract

We perform the baseline and energy optimization of the Neutrino Factory including the latest simulation results on the magnetized iron detector (MIND). We also consider the impact of  $\tau$  decays, generated by  $\nu_\mu \rightarrow \nu_\tau$  or  $\nu_e \rightarrow \nu_\tau$  appearance, on the mass hierarchy, CP violation, and  $\theta_{13}$  discovery reaches, which we find to be negligible for the considered detector. For the baseline-energy optimization for small  $\sin^2 2\theta_{13}$ , we qualitatively recover the results with earlier simulations of the MIND detector. We find optimal baselines of about 2 500 km to 5 000 km for the CP violation measurement, where now values of  $E_\mu$  as low as about 12 GeV may be possible. However, for large  $\sin^2 2\theta_{13}$ , we demonstrate that the lower threshold and the backgrounds reconstructed at lower energies allow in fact for muon energies as low as 5 GeV at considerably shorter baselines, such as FNAL-Homestake. This implies that with the latest MIND analysis, low- and high-energy versions of the Neutrino Factory are just two different versions of the same experiment optimized for different parts of the parameter space. Apart from a green-field study of the updated detector performance, we discuss specific implementations for the two-baseline Neutrino Factory, where the considered detector sites are taken to be currently discussed underground laboratories. We find that reasonable setups can be found for the Neutrino Factory source in Asia, Europe, and North America, and that a triangular-shaped storage ring is possible in all cases based on geometrical arguments only.

---

<sup>a</sup>Email: Sanjib.Agarwalla@ific.uv.es

<sup>b</sup>Email: pahuber@vt.edu

<sup>c</sup>Email: jtang@physik.uni-wuerzburg.de

<sup>d</sup>Email: winter@physik.uni-wuerzburg.de

# 1 Introduction

Neutrino oscillation experiments have provided compelling evidence that the active neutrinos are massive particles [1], pointing towards physics beyond the Standard Model. In a three-generation scenario, there are two characteristic mass squared splittings ( $\Delta m_{31}^2, \Delta m_{21}^2$ ) and three mixing angles ( $\theta_{12}, \theta_{13}, \theta_{23}$ ) as well as a CP violating phase  $\delta_{\text{CP}}$  affecting neutrino oscillations. A global fit of solar, atmospheric, accelerator and reactor neutrino oscillation experiments, yields the following parameter ranges for the oscillation parameters at the  $1\sigma$  level [2]:  $\Delta m_{21}^2 = (7.59 \pm 0.20) \times 10^{-5} \text{ eV}^2$ ,  $|\Delta m_{31}^2| = (2.46 \pm 0.12) \times 10^{-3} \text{ eV}^2$ ,  $\theta_{12} = (34.4 \pm 1.0)^\circ$ ,  $\theta_{23} = (42.8_{-2.9}^{+4.7})^\circ$  and  $\theta_{13} = (5.6_{-2.7}^{+3.0})^\circ$ . Even, within the three flavor framework, there are still unknowns: the mass hierarchy (MH)– $\Delta m_{31}^2 > 0$  (normal ordering) or  $\Delta m_{31}^2 < 0$  (inverted ordering); the value of  $\theta_{13}$ <sup>1</sup>, and whether there is CP violation (CPV) in the lepton sector. The experiment class, which may ultimately address these questions, is the Neutrino Factory [4, 5].

In a Neutrino Factory, neutrinos are produced from muon decays in straight sections of a muon storage ring. The feasibility and a possible design of a Neutrino Factory have been subject of several, extensive international studies, such as in Refs. [6–8]. The International Neutrino Factory and Superbeam Scoping Study [8–10] has laid the foundations for the currently ongoing Design Study for the Neutrino Factory (IDS-NF) [5]. The goal of the IDS-NF is to present a conceptual design report, a schedule, a cost estimate, and a risk assessment for a Neutrino Factory facility by 2013. The IDS-NF defines a first-version baseline setup of a high energy neutrino factory with  $E_\mu = 25 \text{ GeV}$  and two baselines  $L_1 \simeq 3\,000 - 5\,000 \text{ km}$  and  $L_2 \simeq 7\,500 \text{ km}$  (the “magic” baseline [11]) served by two racetrack-shaped storage rings, with a muon energy of 25 GeV (for optimization questions, see, *e.g.*, Refs. [12–19]). This setup has been demonstrated to have excellent  $\sin^2 2\theta_{13}$  reaches for addressing the open questions in the three flavor scenario [17], to be robust against many potential new physics effects [19, 20] or systematical errors [21], and to be useful for degeneracy resolution independently of the finally achieved luminosity [11]; for the physics case for the very long baseline, see also Ref. [18].

The appearance signal in a neutrino factory consists of so called wrong-sign muons (*e.g.*, from  $\bar{\nu}_e \rightarrow \bar{\nu}_\mu$ ) and therefore a detector which is capable of measuring the charge sign of muons is required in order to distinguish this signal from the right-sign (*e.g.*, from  $\nu_\mu \rightarrow \nu_\mu$ ) muon background. The most straightforward solution towards a high fidelity muon charge measurement is a magnetized iron detector (MIND). With a MIND, the achievable levels of muon charge identification allow for CP violation measurements in the muon neutrino appearance channels [13, 14].

The optimal MIND detector has backgrounds (such as from neutral currents or charge misidentification) at the level of about  $10^{-3}$  to  $10^{-4}$ , and the potential to measure the muon charges at relatively low energies down to a few GeV. The importance of the precise location of the detection threshold was discussed in detail in Refs. [17, 22]. As the design of the Neutrino Factory matures, more refined detector simulations have become available [23, 24], especially in comparison to the IDS-NF baseline 1.0 [5]. Compared to the older analyzes,

---

<sup>1</sup> Note, that recent hints for  $\theta_{13} > 0$  [3] are inconclusive and need to await more experimental data.

these new simulations provide the detector response in terms of migration matrices mapping the incident to the reconstructed neutrino energy for all individual signal and background channels. An optimization of the cuts has led to a lower threshold and higher signal efficiencies than in previous versions, while the background level has been maintained in the most recent analysis [24]. In addition, separate detector response functions for neutrinos and anti-neutrinos are available, and it turns out that the  $\bar{\nu}_\mu$  detection efficiency is better than the  $\nu_\mu$  detection efficiency, which partially compensates for the different cross sections.<sup>2</sup> The MIND detector has been studied in Ref. [23, 24] as generic neutrino factory detector and a specific detector of similar type is proposed for the India-based Neutrino Observatory (INO) to measure atmospheric neutrinos [25]. The detector at INO may serve as a Neutrino Factory far detector at a later stage.

Most recently, the background from  $\tau$  decays was discussed for disappearance [26] and appearance [27] channels. These taus arise from charged current interaction of  $\nu_\tau$  which are due to oscillation, *e.g.*, for  $\mu^+$  stored:

$$\text{App.: } \nu_e \rightarrow \nu_\tau \rightarrow \tau^- \xrightarrow{17\%} \mu^- \text{ (background) versus } \nu_e \rightarrow \nu_\mu \rightarrow \mu^- \text{ (signal)} \quad (1)$$

$$\text{Disapp.: } \bar{\nu}_\mu \rightarrow \bar{\nu}_\tau \rightarrow \tau^+ \xrightarrow{17\%} \mu^+ \text{ (background) versus } \bar{\nu}_\mu \rightarrow \bar{\nu}_\mu \rightarrow \mu^+ \text{ (signal)} \quad (2)$$

The reason for these muons to contribute to the background is that the MIND cannot resolve the second vertex from the  $\tau$  decay, in contrast to OPERA-like emulsion cloud chamber (ECC) [28]. In principle, the muons from  $\tau$  decays carry information which may be used for the standard oscillation [29, 30] or new physics [31] measurements.

An alternative version of the Neutrino Factory with respect to the IDS-NF baseline has been proposed in Refs. [32–37]. The key difference is to replace the MIND with a magnetized totally active scintillator detector (TASD). The TASD, being fully active, has a lower threshold and better energy resolution. The better detector performance and an optimization of the front-end increasing the intensity have allowed a version of the Neutrino Factory with  $E_\mu \sim 5$  GeV and a baseline possibly as short as  $L \simeq 1\,300$  km, corresponding to FNAL-Homestake. This version is usually called “low energy Neutrino Factory” (LENF) and it is found that the LENS has especially good performances for large  $\sin^2 2\theta_{13}$ . In addition, the performance of a TASD allows to exploit the “platinum channel” ( $\nu_\mu \rightarrow \nu_e$ ), however it turns out that it is of little practical value [36].

The recent simulation results for the MIND have made the performance margin between TASD and MIND considerably smaller and therefore, we will show that the distinction between the low- and high-energy Neutrino Factory is somewhat artificial and merely corresponds to two extreme corners of a common parameter space.

The phenomenological discussion of the Neutrino Factory has so far been performed mostly in an abstract baseline-energy space. While the energy is a continuous variable, it is not obvious that all baselines can be realized from any accelerator site. Therefore, we will present a comparison of physics performances for a judicious choice of accelerator and detector locations. It seems unlikely that a machine of the size and complexity of the accelerator part of a Neutrino Factory would be built on a green-field site and therefore, we assume

---

<sup>2</sup>The difference in neutrino and anti-neutrino response is due to the different  $y$ -distributions [24].

that it will be co-located with an existing, large accelerator facility. To be specific we consider: CERN, the Fermi National Accelerator Laboratory (FNAL), the Japan Proton Accelerator Research Complex (J-PARC), and the Rutherford Appleton Laboratory (RAL) as potential accelerator sites [10]. For the choice of potential detector sites the issue is less clear-cut, since, at the current stage, there is little information on the required amount of rock overburden for a MIND (or T ASD) to perform satisfactorily. Therefore, we make the conservative choice and assume that a Neutrino Factory far detector requires a similar amount of rock overburden as other neutrino experiments do. Under this assumption, a natural choice of candidate detector sites is given by candidate detector sites for other neutrino experiments. Fortunately, lists of candidate sites for general neutrino experiments have been compiled for the US in response to the National Science Foundation (NSF) call for proposals for a Deep Underground Science and Engineering Laboratory (DUSEL) [38] and for Europe in the context of the Large Apparatus studying Grand Unification and Neutrino Astrophysics (LAGUNA) [39] study. In North America, we consider eight locations: Soudan, WIPP, Homestake, SNOLAB, Henderson, Icicle Creek, San Jacinto, and Kimballton. In Europe, under LAGUNA, there are seven possible candidate sites: Pyhäsalmi in Finland, Slanic in Romania, Boulby in UK, Canfranc in Spain, Fréjus in France, SUNLAB in Poland, and Umbria in Italy. Along with these seven sites, we also consider Gran Sasso National Laboratory (LNGS) in Italy and Gran Canaria in Spain. We will complement these lists of detector sites by the Asian facilities: the Kamioka mine in Japan, the proposed Chinese underground laboratory at CJPL, YangYang in Korea, as well as INO in India.

This paper is organized as follows: We describe our methods and implementation in Sec. 2. After that, we update the simultaneous optimization of baseline and muon energy in Sec. 3 in a green-field scenario. In Sec. 4, we discuss the selection of specific sites, the site geometry, and the possibility to use a triangular-shaped storage ring. Furthermore, in Sec. 5, we quantify site-specific performance of the Neutrino Factory. Finally, we summarize and draw our conclusions in Sec. 6. Details for the assumptions for the individual accelerator and detector sites can be found in Appendix A. The sensitivity curves for all possible considered site combinations are given Appendix B. The individual data files for the curves are available for download at Ref. [40].

## 2 Simulation method and performance

In this section we describe our simulation method and we show the difference to the IDS-NF 1.0 in terms of event rates. We also compare the performance resulting from the different detector simulations, and we compare the performance between one and two baselines.

### 2.1 Simulation method

For the simulation of the Neutrino Factory, we use the GLoBES software [41, 42]. The description of the experiment is based on Refs. [17, 22], where we use the parameters from the IDS-NF baseline setup 1.0 (IDS-NF 1.0) described in Ref. [5] (note number IDS-NF-002). The detector description of this setup is based on Ref. [9], which has been updated

in Refs. [23, 24]. In this section, we compare these three detector descriptions, whereas we use only the most recent version, Ref. [24], in the following sections. IDS-NF 1.0 uses two magnetized iron calorimeters (fiducial mass 50 kt) at  $L = 4000$  km and  $L = 7500$  km. There are two racetrack-shaped storage rings pointing towards these detectors, with a luminosity of  $2.5 \times 10^{20}$  useful muon decays per polarity, decay straight, and year, *i.e.*,  $10^{21}$  useful muon decay per year. We assume a running time of 10 years, *i.e.*,  $10^{22}$  useful muon decay in total. The parent muon energy is assumed to be  $E_\mu = 25$  GeV. The considered oscillation channels are:

$$\nu_\mu \text{ appearance: } \nu_e \rightarrow \nu_\mu \text{ for } \mu^+ \text{ stored,} \quad (3)$$

$$\bar{\nu}_\mu \text{ appearance: } \bar{\nu}_e \rightarrow \bar{\nu}_\mu \text{ for } \mu^- \text{ stored,} \quad (4)$$

$$\nu_\mu \text{ disappearance: } \nu_\mu \rightarrow \nu_\mu \text{ for } \mu^- \text{ stored,} \quad (5)$$

$$\bar{\nu}_\mu \text{ disappearance: } \bar{\nu}_\mu \rightarrow \bar{\nu}_\mu \text{ for } \mu^+ \text{ stored.} \quad (6)$$

Since the luminosity changes if one or two storage rings are required, *i.e.*, one or two baselines are operated, and the efficiency of a triangular-shaped ring, which will discuss later, is different, it is convenient to re-parameterize luminosity in terms of a scale factor (SF) [37]: SF=1 corresponds to the above mentioned parameters  $2.5 \times 10^{20}$  useful muon decays per polarity, decay straight, and year. If only one baseline is needed, then all muons can be injected in the same storage ring, and SF=2. If, on the other hand, a storage ring with a different geometry (such as a triangle) is used to point towards the two baselines simultaneously, all muons will be injected into this ring, but the straight length towards each detector will be smaller than in the racetrack case, *i.e.*,  $0 < \text{SF} < 2$  in general. The scale factor is then convenient to parameterize the obtained luminosity relative to the IDS-NF baseline setup: SF>1: higher luminosity, SF<1: lower luminosity. Note that, in principle, the SF can, for lower  $E_\mu$ , also be increased by a re-optimization of the front-end and generally will increase for lower energies due to the reduced decay losses during acceleration. For example, a SF=2.8 for a low energy 4 GeV Neutrino Factory has been obtained in Ref. [35] compared to SF=2.0. We will not consider this type of effect, since it depends on the accelerator complex in a non-trivial fashion.

For the updated detector simulations, we use the migration matrices mapping the incident to the reconstructed neutrino energies for all individual signal and background channels, which can be directly implemented into GLoBES. Note that charge mis-identification, (electron) flavor mis-identification and neutral current backgrounds are included. For the binning, we then follow Ref. [23, 24], where the migration matrices for the appearance channels are given. For the disappearance channels, we use the same matrices.<sup>3</sup> In addition, we increase the number of sampling points for high energies to avoid aliasing. This implementation will be used throughout the remainder of this paper, unless indicated otherwise. It is denoted by the label “new-NF”. Note that we also include signal (2.5%) and background (20%) normalization errors, uncorrelated among all oscillation channels.

For the  $\nu_\tau$  contamination, we use the migration matrix from Ref. [27] for both the  $\nu_e \rightarrow \nu_\tau$

---

<sup>3</sup>That is somewhat on the conservative side, since we require charge identification and better results may be obtained with an event sample without charge identification [17].

	Signal	NC bckg	CC bckg	$\nu_\tau$ bckg
$\nu_\mu$ (app)	7521	20	25	142
$\bar{\nu}_\mu$ (app)	924	45	39	13
$\nu_\mu$ (disapp)	$4.0 \times 10^5$	31	-	8154
$\bar{\nu}_\mu$ (disapp)	$2.4 \times 10^5$	8	-	4337

**Table 1:** The expected event rates for new-NF $\tau$  in a 50kt detector at a 4000 km baseline with a muon energy of 25 GeV. The chosen oscillation parameters are taken from Eq. (7) with  $\theta_{13} = 5.6^\circ$  and  $\delta_{\text{CP}} = 0$ .

and  $\nu_\mu \rightarrow \nu_\tau$  channels, since it only depends on characteristics of the  $\tau$  decays. Note that, since the binning given in there is different from Refs. [23, 24], we had to re-bin this matrix carefully. As an important consequence, all events below 2 GeV are collected in the lowest bin. We also apply the muon kinematic cuts for the muons from the  $\tau$  decays as for the golden channel, following Ref. [27]. In a more refined approach, one may want to have the migration matrices from incident  $\nu_\tau$  energy to reconstructed  $\nu_\mu$  energy directly. This setup will be denoted as “new-NF $\tau$ ” and it contains everything in new-NF plus the muons from  $\tau$  decays. As we will show new-NF $\tau$  produces practically the same results as new-NF<sup>4</sup>.

The input oscillation parameters are taken as follows [2], unless noted otherwise:

$$\begin{aligned} \theta_{12} = 34.4^\circ, \quad \theta_{13} = 5.6^\circ, \quad \theta_{23} = 42.8^\circ \\ \Delta m_{21}^2 = 7.59 \times 10^{-5} \text{ eV}^2, \quad |\Delta m_{31}^2| = 2.46 \times 10^{-3} \text{ eV}^2. \end{aligned} \quad (7)$$

We impose external  $1\sigma$  errors on  $\Delta m_{21}^2$  (4%) and  $\theta_{12}$  (4%) and on  $\Delta m_{31}^2$  (10%) and  $\theta_{23}$  (10%) as conservative estimates<sup>5</sup> for the current measurement errors [2]. We also include a 2% matter density uncertainty [43, 44]. Unless noted otherwise, we simulate the normal hierarchy.

## 2.2 Event rate comparison

In Fig. 1, we compare the event rates of the latest detector simulation new-NF (thick solid curves) with IDS-NF 1.0 (thin solid curves) for the four different oscillation channels as given in the plot legend.

IDS-NF 1.0 (thin curves) did not use any migration matrices and this is reflected in the background shape, both neutral current (NC) and charged current (CC), which closely follows the signal shape. The signal shape of IDS-NF 1.0 is quite similar to the one of new-NF, indicating that migrations are not large for the signal, which is not surprising since energy reconstruction works well for the signal events. The background shapes, on

<sup>4</sup>This statement is true only for the performance indicators used in this paper, which all focus on the appearance channel, and will most likely not apply to precision measurements of the atmospheric neutrino parameters in the disappearance channels as indicated in Ref. [26].

<sup>5</sup>Here we expect that the best measurement of the atmospheric parameters comes from the Neutrino Factory in the near future. However, it is useful to add the current information on the atmospheric parameters to speed up the marginalization and degeneracy finding.

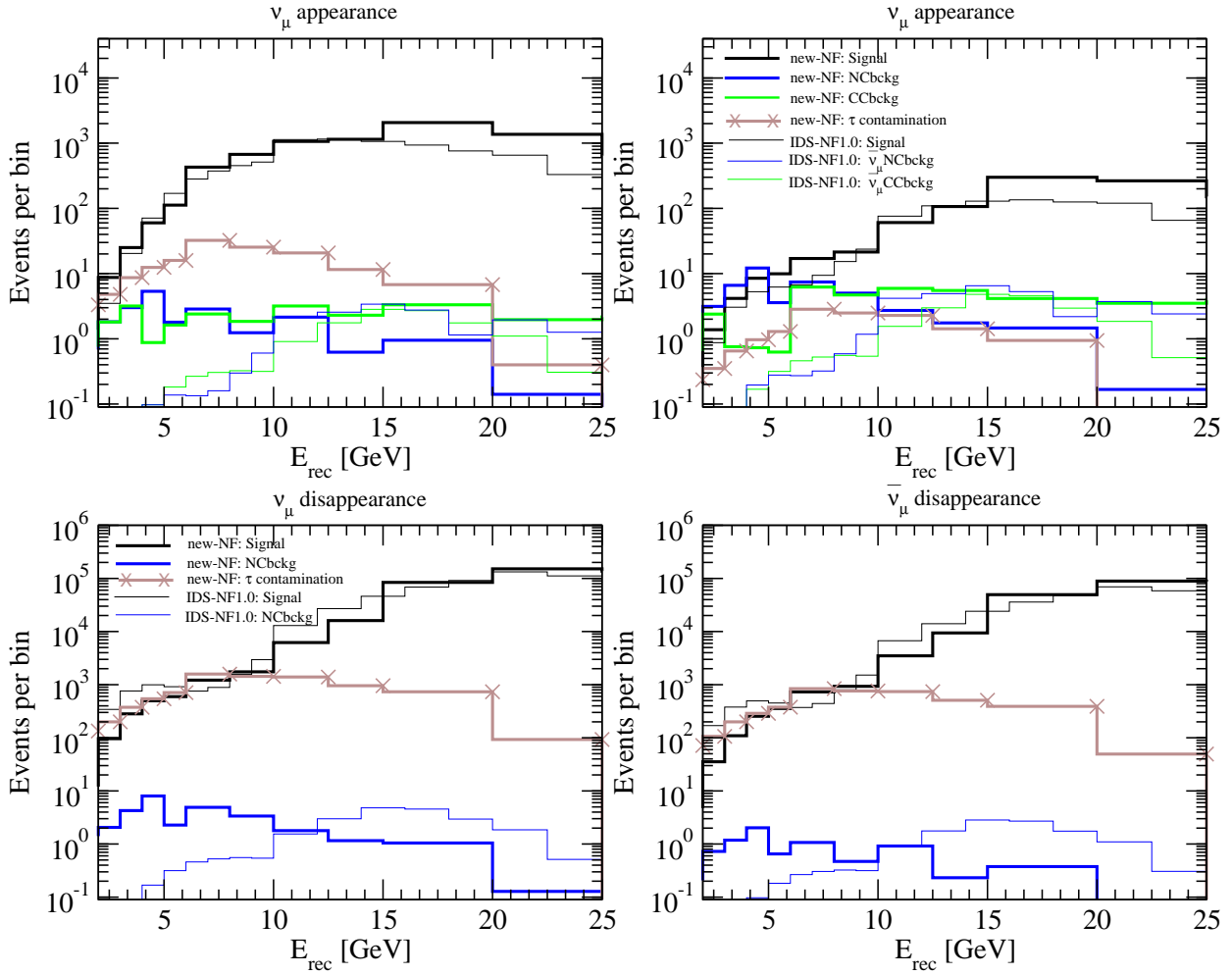


**Figure 1:** A comparison of the event rate spectra between new-NF [24] (thick curves), including backgrounds from  $\nu_\tau$  [26,27], and IDS-NF 1.0 (thin curves) for the different oscillation channels as given in the plot legend. The chosen oscillation parameters are taken from Eq. (7) with  $\delta_{CP} = 0$ . The muon energy is 25 GeV and the detector mass is 50kt at a baseline of 4000 km.

the other hand, differ substantially between IDS-NF 1.0 and new-NF, since here migrations are non-negligible. In particular for the NC background, we observe that for new-NF (thick curves) it is quite peaked at low energies. This phenomenon is known as “feed-down”: for a given incoming neutrino energy, there will be less energy deposited in the detector in a NC event than in a CC event, simply because a neutrino is leaving the detector carrying away a sizable fraction of the incoming energy. If a NC event is mis-identified as being a CC event<sup>6</sup>, then the CC event kinematics will be used for energy reconstruction, which assumes that  $E_\nu^{\text{rec}} = E_{\text{lepton}}^{\text{rec}} + E_{\text{hadrons}}^{\text{rec}}$ . This results in a systematic downward bias in the reconstructed energy for NC background events. This feed-down is the strongest effect of migration and thus has potential impact on the energy optimization, since it penalizes neutrino flux at high energies, where there is little oscillation but a large increase in feed-down background. Also, for muons from  $\tau$  decays there is a strong feed-down for a similar reason: in the decay of a  $\tau$  there will be two additional neutrinos which leave the detector. Here, the disruptive effect of high energies is even more pronounced, since the  $\nu_\tau$  CC cross section is a steeply increasing function of neutrino energy up to about 30 GeV.

In summary, the CC backgrounds in new-NF pile-up at lower energies. These low energy events are relevant for degeneracy resolution, especially for intermediate values of  $\sin^2 2\theta_{13} \sim 10^{-4} - 10^{-2}$ . However, the oscillation peak in vacuum would be at about 10 GeV, and matter effects are most important at about 8 GeV, which need to be covered especially for small  $\sin^2 2\theta_{13}$ , where the event rates otherwise rapidly decrease with distance. The backgrounds from  $\tau$  decay in new-NF  $\tau$  tend to collect around 8 GeV and may present an immediate problem for all values of  $\sin^2 2\theta_{13}$ . Therefore, it is not quite clear that high muon energies are preferred everywhere in the parameter space, and one may suspect that the baseline-muon energy optimization may be a complicated function of the detector response.

### 2.3 Performance and impact of $\nu_\tau$ contamination

Neutral current backgrounds do not carry any information about flavor conversions of active neutrinos and therefore are detrimental to oscillation searches. The muons from  $\tau$  decays, on the other hand, do arise from oscillation and they are a sign of appearance of a new flavor,  $\tau$ , in a beam otherwise devoid of this flavor. The background arising from  $\nu_\tau$  as defined in Eq. (1) (appearance channels) and Eq. (2) (disappearance) are shown as gray (brown) solid curves in Fig. 1. In all channels, they are the largest source of background. It is, however, not clear from the beginning whether this is a benefit or a curse, since this oscillating background carries information on the oscillation parameters. In particular, the low energy parts, which actually stem from much higher incident neutrino energies, may carry complementary information to the high energy signal; since the resulting energy distribution is different they may be separated on a statistical basis. For example, the  $\nu_\mu$  appearance probability is given, expanded to second order in  $\sin 2\theta_{13}$  and the hierarchy parameter  $\alpha \equiv \Delta m_{21}^2 / \Delta m_{31}^2 \simeq 0.03$ , as [13, 45, 46]:

$$P_{e\mu} \simeq \sin^2 2\theta_{13} \sin^2 \theta_{23} \frac{\sin^2[(1 - \hat{A})\Delta_{31}]}{(1 - \hat{A})^2}$$

---

<sup>6</sup>Otherwise, it would not be a background event.



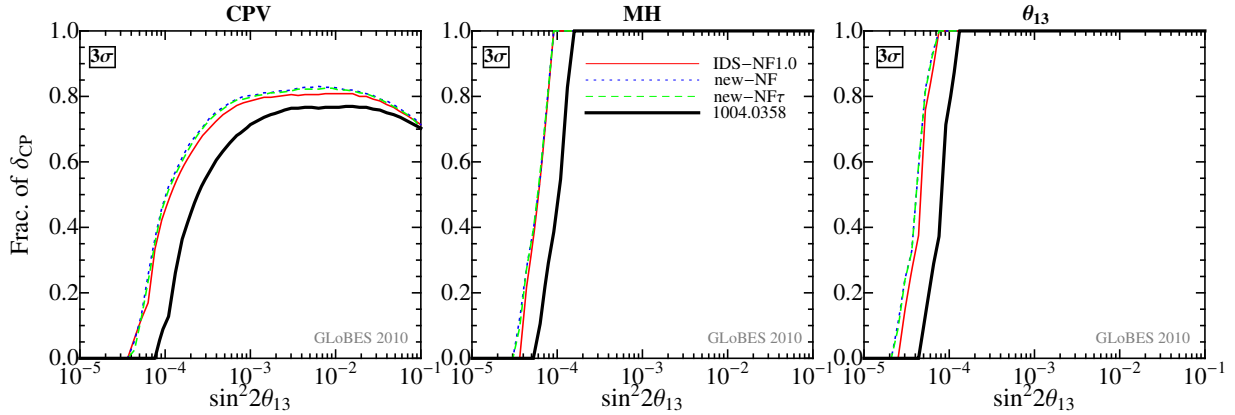


**Figure 2:** A comparison of the discovery reach of CPV, MH, and  $\theta_{13}$  at the  $3\sigma$  CL among different detector simulations. The label “IDS-NF” refers to the detector in the IDS-NF baseline setup 1.0 [5]. The simulation with the migration matrices from [23] is indicated by the label “1004.0358”. The label “new-NF” refers to most up-to-date detector simulation in Ref. [24]. The  $\nu_\tau$  contaminations in the appearance and disappearance channels are, in addition, included in “new-NF $\tau$ ” [26, 27]. Here a combination of two baselines 4000 km and 7500 km with two 50 kt MIND detectors is assumed.

$$\begin{aligned}
& \pm \alpha \sin 2\theta_{13} \sin \delta_{\text{CP}} \sin 2\theta_{12} \sin 2\theta_{23} \sin(\Delta_{31}) \frac{\sin(\hat{A}\Delta_{31})}{\hat{A}} \frac{\sin[(1-\hat{A})\Delta_{31}]}{(1-\hat{A})} \\
& + \alpha \sin 2\theta_{13} \cos \delta_{\text{CP}} \sin 2\theta_{12} \sin 2\theta_{23} \cos(\Delta_{31}) \frac{\sin(\hat{A}\Delta_{31})}{\hat{A}} \frac{\sin[(1-\hat{A})\Delta_{31}]}{(1-\hat{A})} \\
& + \alpha^2 \cos^2 \theta_{23} \sin^2 2\theta_{12} \frac{\sin^2(\hat{A}\Delta_{31})}{\hat{A}^2}
\end{aligned} \tag{8}$$

with  $\Delta_{31} \equiv \Delta m_{31}^2 L / (4E)$  and  $\hat{A} = \pm 2\sqrt{2} E G_F n_e / \Delta m_{31}^2$ . The signs in the second term and  $\hat{A}$  are positive for neutrinos and negative for anti-neutrinos. For  $P_{e\tau}$ , the channel which controls the background in Eq. (1), flip the sign of the second and third terms and replace in the first and fourth terms  $\sin^2 \theta_{23} \leftrightarrow \cos^2 \theta_{23}$ . For maximal atmospheric mixing, only the signs of the second and third terms change. Now consider, for instance, the magic baseline  $L \simeq 7500$  km where, by definition,  $\sin(\hat{A}\Delta_{31}) \simeq 0$  [11]. In this case, only the first term survives, which is the same for the signal and for the background, which means that it adds to the  $\sin^2 2\theta_{13}$  and MH sensitivity. For the short baseline used for the CPV measurement, the sign of the second and third terms are different between  $P_{e\mu}$  and  $P_{e\tau}$ , which means that the effects of  $\delta_{\text{CP}}$  are, naively, reduced by the  $\nu_\tau$  background. However, note that the background is reconstructed at lower energies, which means that one can, in principle, distinguish the two channels. It is therefore, without numerical simulation, not obvious if the  $\nu_\tau$  contaminations improve or deteriorate the sensitivities.

The physics performance arising from the different detector simulations for the CPV, MH, and  $\theta_{13}$  discovery reaches are shown in Fig. 2. Here “IDS-NF 1.0” refers to the detector performance of the IDS-NF baseline setup 1.0 [5]. The results in the figure demonstrate that the performance based on the detector simulation presented in Ref. [23] (thick solid curves) is worse. The main reason, we were able to identify, is significantly higher backgrounds from

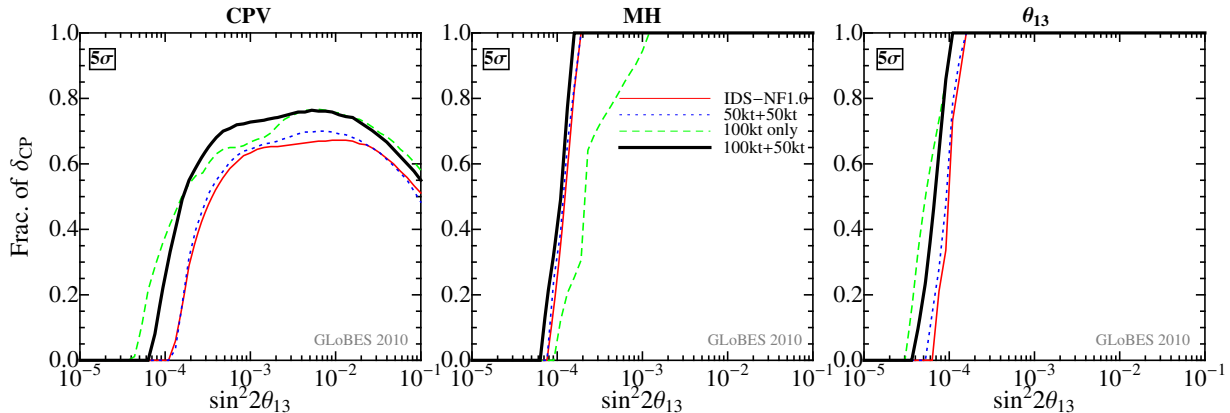


**Figure 3:** A comparison of the discovery reach of CPV, MH, and  $\theta_{13}$  at the  $5\sigma$  CL among different experimental setups: “50kt+50kt” refers to a combination of 50 kt MIND at 4000 km and 50 kt MIND at 7500 km (SF=1), “100kt only” to a 100 kt MIND at 4000 km (SF=2), “100kt+50kt” to the combination of a 100 kt MIND at 4000 km and 50 kt MIND at 7500 km (SF=1). All these setups use the most up-to-date detector simulation new-NF [24]. “IDS-NF 1.0” refers to IDS-NF baseline setup 1.0, *i.e.*, the combination of 50 kt MIND at 4000 km and 50 kt MIND at 7500 km (SF=1), using no migration matrices [5] (note number IDS-NF-002), to be compared to the dotted curves.

charge mis-identification than in the IDS-NF 1.0. The most up-to-date detector simulation is presented in Ref. [24] (dotted curves) and this setup is labeled new-NF, for which the performance is slightly better than for the IDS-NF 1.0. In this case, the signal efficiencies and threshold are improved compared to IDS-NF 1.0, while the background level is maintained. One of the main differences with respect to Ref. [23] is the inclusion of quasi-elastic events which improves the signal efficiency at low energies. The effect of the migration of the backgrounds does not have a large impact on the discovery reaches. This may not be true for precision studies of the atmospheric oscillation parameters, however, a detailed answer to this question is beyond the scope of the current paper. If, in addition, the contributions from the  $\nu_\tau$  are included, new-NF $\tau$  (dashed curves), there is hardly any effect on the performances. Note, that the relative impact of  $\tau$  decays does depend on the underlying detector parameters and this illustrates that it is difficult to predict the effect of the  $\nu_\tau$  without numerical simulation. In any case, the absence of a significant difference in performances between new-NF and new-NF $\tau$  is in agreement with the results presented in Ref. [27] and therefore, we will not further consider  $\tau$  decays and the resulting backgrounds.

Other questions to be addressed in the context of the updated detector simulation are the quantitative comparison between one and two baselines, and the impact of a larger detector at the shorter baseline. We discuss these in Fig. 3, where several versions of the updated detector are compared with the IDS-NF 1.0. Note that the scale factor (SF) has been adjusted for the assumed racetrack storage rings to correct for the larger number of useful muon decays during the single baseline operation. In addition, note that this figure is shown at the  $5\sigma$  CL, compared to the previous, to make the impact of degeneracies clearer. From the comparison of the IDS-NF 1.0 and the corresponding 50kt+50kt curves using new-NF confirm the earlier result, note that there is not much difference in performance. A possible alternative setup is to operate a single 100 kt detector at the 4000 km baseline,

this configuration is labeled “100kt only”. This configuration actually exhibits better performances for CPV and the  $\theta_{13}$  discovery because of the factor of two higher luminosity using the racetrack-shaped storage rings. In this case, the complementary information at the 7500 km baseline is replaced by high statistics at the short baseline. Note, however, that the MH discovery reach is significantly worse, and that degeneracies affect the shape of the CPV curve. The setup “100kt+50kt”, where there is a 100 kt detector at 4000 km and one 50kt at 7500 km, can easily resolve the degeneracies at about  $\sin^2 2\theta_{13} \sim 10^{-3}$  in the CPV discovery reach, while the MH and  $\theta_{13}$  discovery reaches are comparable. In this case, SF=1, which means that this setup in fact only has 75% of the exposure of the “100kt only” version. Therefore, the two baselines are synergistic in the sense of Ref. [47], *i.e.*, for the same exposure, the baseline combination clearly performs better. However, if one sticks to the racetrack geometry of the storage rings, the one baseline operation may be more efficient. For a triangular shaped ring, which we will discuss later, this argument changes, because the second baseline is available anyway. The question of the necessity of the magic baseline remains open. Especially in the context of new physics and surprises, such as a lower than expected machine luminosity, it provides a robust alternative.

In the following, now that we have quantified the impact on the performance, we will only consider the setup with the updated migration matrices from Ref. [24], *i.e.*, new-NF. Whenever we refer to “IDS-NF”, we will actually mean the IDS-NF parameters ( $E_\mu = 25$  GeV, 4000 km + 7500 km), while the detector simulation is new-NF. We will not consider the  $\nu_\tau$  contribution anymore, partially because it has been shown not to have a significant impact on the discussed performance indicators, partially because it will need to be quantified within the same detector simulation as the signal and other backgrounds in the future.

### 3 Optimization of a green-field setup, low versus high energy Neutrino Factory?

Here we study the optimization of a green-field setup, which means that no particular accelerator and detector sites are chosen and that the baselines and muon energy are not constrained. The optimization is performed using the migration matrices from Ref. [24]. Now that the detection threshold has improved, we are especially interested if the new MIND detector can interpolate between low and high energy Neutrino Factory.

First of all, consider that  $\sin^2 2\theta_{13}$  is not found before the Neutrino Factory operation. Assume that, in this case, one wanted to optimize for the reach in  $\sin^2 2\theta_{13}$ , *i.e.*, CPV, MH, and  $\theta_{13}$  should be discovered for as small as possible true values of  $\sin^2 2\theta_{13}$ . For the sake of simplicity, we choose maximal CP violation  $\delta_{\text{CP}} = \pi/2$  for the true  $\delta_{\text{CP}}$ .<sup>7</sup> We show in Fig. 4 the discovery reach in  $\sin^2 2\theta_{13}$  for maximal CP violation, MH, and  $\theta_{13}$  as a function of baseline and  $E_\mu$ . The contours show the reach in (true)  $\sin^2 2\theta_{13}$  for which the different quantities will be discovered at the  $3\sigma$  CL. This figure is to be compared

---

<sup>7</sup>Other, more technical versions, are choosing the “typical value of  $\delta_{\text{CP}}$ ” (the median of the distribution in  $\delta_{\text{CP}}$ ), corresponding to a fraction of  $\delta_{\text{CP}}$  of 50%, or a different certain fraction of  $\delta_{\text{CP}}$ . At least for CPV, our choice corresponds to the most optimistic case.

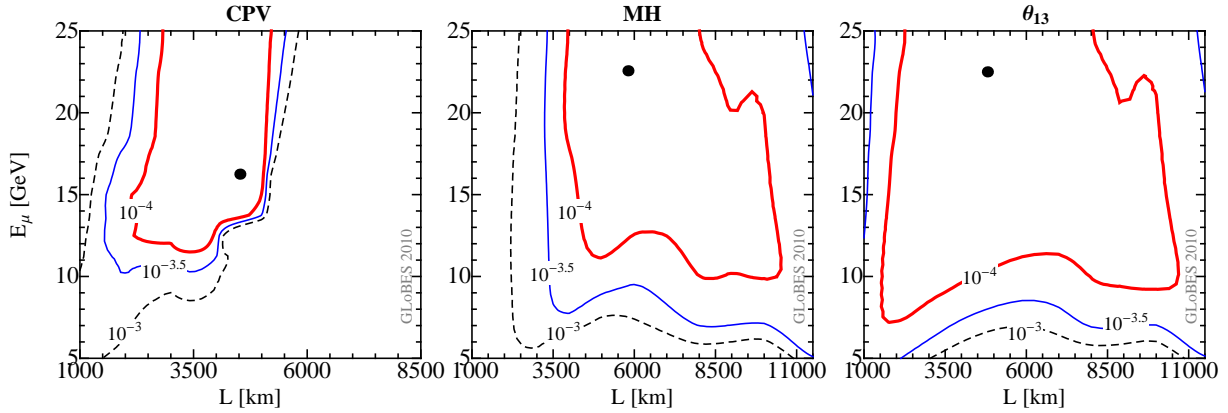


**Figure 4:** Discovery reach in  $\sin^2 2\theta_{13}$  for maximal CP violation, MH, and  $\theta_{13}$  as a function of baseline and  $E_\mu$ . The contours show for how small (true)  $\sin^2 2\theta_{13}$  the different quantities will be discovered at the  $3\sigma$  CL, where maximal CP violation  $\delta_{\text{CP}} = \pi/2$  is chosen as a true value in all cases. The best reaches for baseline and  $E_\mu$  are marked by dots: (4519,16.25), (5805,22.57) and (4800,22.50) followed by their optimal sensitivity of  $\sin^2 2\theta_{13}$  at  $10^{-4.8}$ ,  $10^{-4.5}$  and  $10^{-4.5}$ . Here SF=1 is used with one 50 kt detector.

to Figs. 5 and 6 of Ref. [17] for the respective  $\delta_{\text{CP}}$  and an older version of the detector simulation. Here the qualitative features are clearly recovered: The CPV discovery requires a 2 500 km to 5 000 km baseline and  $E_\mu$  above about 12 GeV. Note that degeneracies are typically unproblematic for this choice of  $\delta_{\text{CP}}$ , whereas for  $\delta_{\text{CP}} = 3\pi/2$ , a second baseline may be required. In addition, note that relatively low  $E_\mu$  are allowed because of the low detection threshold. For the MH discovery, baselines longer than 4 000 km and  $E_\mu$  larger than about 10-12 GeV are needed, since the MSW resonance energy of about 8 GeV is to be covered. Here even longer baselines are preferred for different values of  $\delta_{\text{CP}}$ . For the  $\theta_{13}$  discovery, we find an extremely wide baseline and energy range, giving the least constraints. However, note again that this result depends on the choice of  $\delta_{\text{CP}}$ . In summary, the result of this optimization, qualitatively, points towards one baseline between 2 500 and 5 000 km for the CPV measurement and one very long baseline for the MH measurement, such as the magic baseline at 7 500 km useful for degeneracy resolution (see Ref. [17] for a more detailed discussion). Because of the optimized detector, lower  $E_\mu$  of down to 12 GeV may be possible. Below, we will discuss how this result changes for specific true values of  $\sin^2 2\theta_{13}$  if all values of  $\delta_{\text{CP}}$  are considered.

From a different perspective, consider that the value of  $\sin^2 2\theta_{13}$  is known, either from an earlier stage experiment or an earlier stage of the Neutrino Factory. In this case, as we have seen in the previous section, the MH discovery is typically not a problem (at least in combination with a longer baseline if  $\sin^2 2\theta_{13}$  is small), and the most interesting question is the optimization of the fraction of  $\delta_{\text{CP}}$  for which CPV can be discovered ( $3\sigma$  CL) as a function of  $L$  and  $E_\mu$  for the single baseline Neutrino Factory. The different panels correspond to different true values of  $\sin^2 2\theta_{13}$ , as given there. From this figure, it is obvious that the optimization strongly depends on the value of  $\sin^2 2\theta_{13}$  chosen. For large  $\sin^2 2\theta_{13} \simeq 10^{-1}$ , shorter baselines and lower energies are preferred. Even  $E_\mu$  as low as 5 GeV at the FNAL-Homestake baseline of about 1 300 km is not far from optimal, which means that the MIND

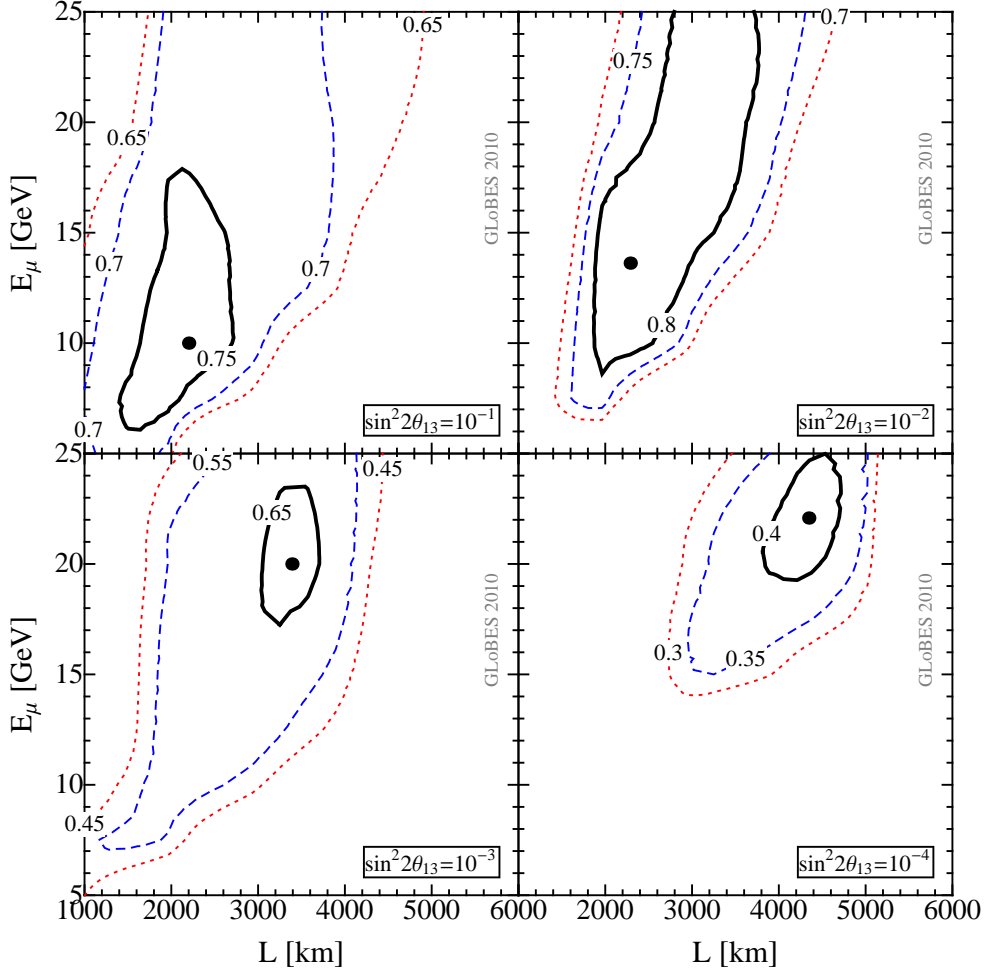


**Figure 5:** Fraction of  $\delta_{CP}$  for which CPV will be discovered ( $3\sigma$  CL) as a function of  $L$  and  $E_\mu$  for the single baseline Neutrino Factory. The different panels correspond to different true values of  $\sin^2 2\theta_{13}$ , as given there. Here SF=1 is used with a 50 kt detector. The optimal performance is marked by a dot: (2200,10.00), (2288,13.62), (3390,20.00) and (4345,22.08) with regard to their best reaches of the fraction of  $\delta_{CP}$  at: 0.77, 0.84, 0.67 and 0.42.

detector approaches the T ASD performance of the low energy Neutrino Factory. Very interestingly, compared to earlier analyses without background migration, too high  $E_\mu$  are in fact disfavored in the large  $\sin^2 2\theta_{13}$  case. Note that neither for the considered detector nor for the T ASD, we find strong evidence supporting the “bi-magic baseline” in Ref. [48], see discussion in Appendix C. For the other extreme,  $\sin^2 2\theta_{13} \simeq 10^{-4}$ , baselines between 4 000 and 5 000 km are preferred with  $E_\mu \simeq 20 - 25$  GeV, which corresponds more to the high energy Neutrino Factory, such as the IDS-NF baseline. Including the other two panels, the optimal region within each panel moves from the lower left on the plots to the upper right as the value of  $\sin^2 2\theta_{13}$  decreases. This means that, depending on the choice of  $\sin^2 2\theta_{13}$ , the optimization results in the low energy Neutrino Factory, the high energy Neutrino Factory, or an intermediate scenario, and that the low and high energy Neutrino Factories are just two versions of the same experiment in different optimization regions. Of course, this discussion is somewhat hypothetical from the practical point of view, since either the next generation(s) of experiments will find  $\sin^2 2\theta_{13}$  or not. If they find  $\sin^2 2\theta_{13}$ , the optimal parameters of the Neutrino Factory can be clearly predicted as a function of the detector response. The FNAL-Homestake low energy Neutrino Factory is one such possible setup for large enough  $\sin^2 2\theta_{13}$  for the MIND detector. If they do not find  $\sin^2 2\theta_{13}$ , one may want to go for the IDS-NF high energy setup, which, in a way, represents the most aggressive but also inclusive option: This version of the Neutrino Factory is optimized for the worst case scenario.

Apart from the single baseline, we show in Fig. 6 the combination with another fixed baseline  $L_2 = 7\,500$  km (in fact, there is typically very little dependence on the exact choice of the second baseline [18]). Note that the muon energy is the same for both baselines. Comparing Fig. 6 with Fig. 5, we find that the optimization of the short baseline hardly changes for very small and very large  $\sin^2 2\theta_{13}$ , whereas the possible baseline windows for intermediate  $\sin^2 2\theta_{13}$  (upper right and lower left panels) become somewhat broader. The energy optimization remains almost unaffected. As far as the absolute performance is concerned, especially for  $\sin^2 2\theta_{13} = 10^{-3}$  and  $\sin^2 2\theta_{13} = 10^{-4}$ , the fraction of  $\delta_{\text{CP}}$  increases because of the degeneracy resolution potential of the second baseline (which is not sensitive to  $\delta_{\text{CP}}$  itself by choosing exactly the magic baseline). For large values of  $\sin^2 2\theta_{13}$ , the second baseline is not required. This again reflects the correspondence to low and high energy Neutrino Factory: the low energy version is typically proposed with one baseline, the high energy version with two baselines.

## 4 Earth geometry, and triangular shaped storage ring?

In this section, we discuss the geometry aspects of specific sites for the high energy Neutrino Factory. The relevant questions for us are:

1. Can we find possible baseline combinations for the high energy Neutrino Factory for the large accelerator laboratories on different continents?
2. Would it be possible to use a single, triangular-shaped storage ring pointing towards both detector locations at the same time?

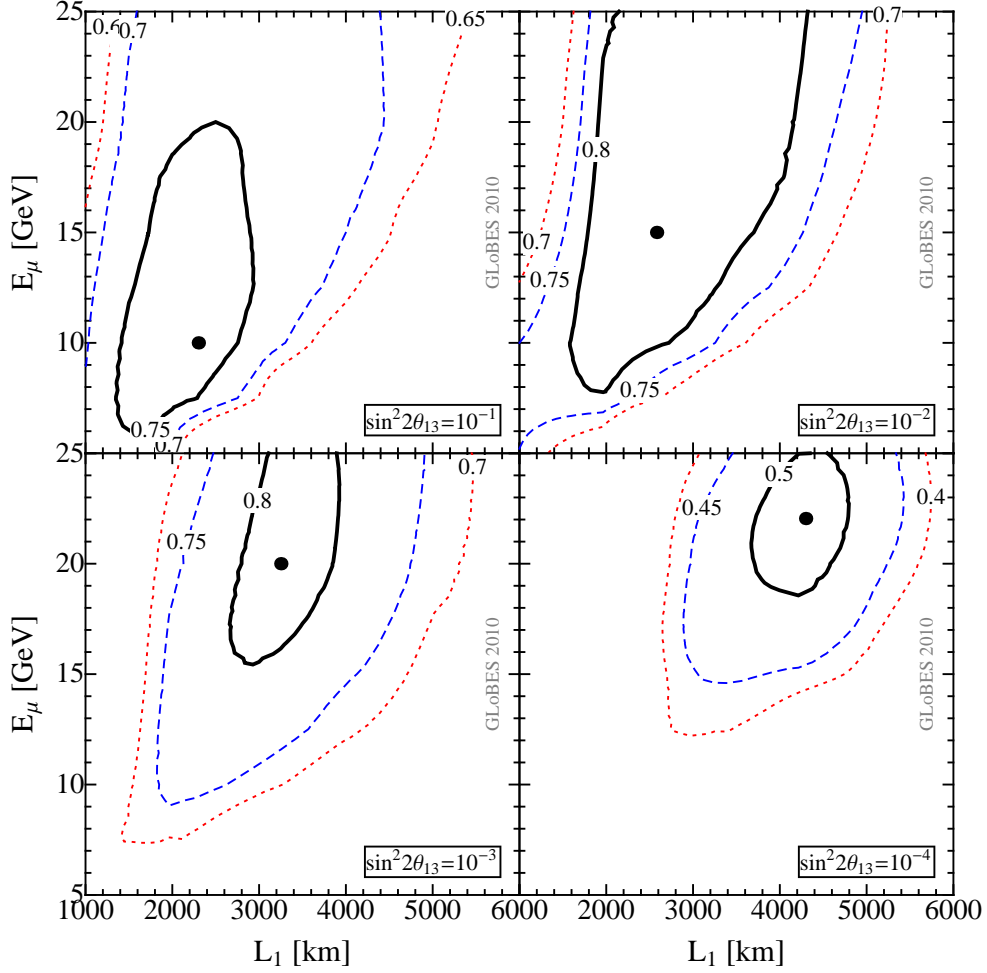


**Figure 6:** Fraction of  $\delta_{CP}$  for which CPV will be discovered ( $3\sigma$  CL) as a function of  $L_1$  and  $E_\mu$  for the two-baseline Neutrino Factory, where  $L_2 = 7500$  km fixed. The different panels correspond to different true values of  $\sin^2 2\theta_{13}$ , as given there. Here SF=1 is used and  $E_\mu$  is assumed to be equal for both baselines. Two 50 kt detectors are used in the simulations. The optimal performance is marked by a dot: (2300,10.00), (2580,15.00), (3250,20.00) and (4297,22.05) followed by their best discovery reach of the fraction of  $\delta_{CP}$  at 0.77, 0.84, 0.81 and 0.51.

	CERN (46.24,6.05)	FNAL (41.85,-88.28)	J-PARC (36.47,140.57)	RAL (51.57,-1.32)
<b>Asia:</b>				
CJPL (28.15,101.71)	7660	10420	3690	7840
Kamioka (36.14,137.24)	8770	9160	300	8640
YangYang (37.77,128.89)	8350	9300	1050	8270
INO (9.92,78.12)	7360	11410	6570	7820
<b>Europe:</b>				
LNGS (42.37,13.44)	730	7350	8840	1510
Pyhäsalmi (63.68,25.98)	2290	6630	7090	2080
Slanic (45.27,25.95)	1540	7780	8150	2110
Boulby (54.56,-0.81)	1050	5980	8480	340
Canfranc (42.76,-0.51)	650	6550	9280	980
Fréjus (45.20,6.67)	130	6830	8900	920
SUNLAB (51.22,16.16)	930	6980	8190	1210
Umbria (42.98,12.64)	640	7280	8830	1420
Gran Canaria (28.39,-16.59)	2780	6240	10570	2850
<b>North America:</b>				
Soudan (47.82,-92.24)	6590	730	8500	5900
WIPP (32.37,-104.23)	8160	1760	8900	7540
Homestake (44.35,-103.77)	7360	1290	8250	6690
SNOLAB (46.47,-81.19)	6090	760	8950	5400
Henderson (39.77,-105.86)	7750	1500	8410	7110
Icicle Creek (47.56,-120.78)	7810	2610	7240	7160
San Jacinto (33.86,-116.56)	8600	2610	8170	8000
Kimballton (37.37,-80.67)	6580	820	9560	5950

**Table 2:** Here we show the baselines between the considered accelerator facilities (columns) and underground laboratories (rows) in kilometers. The latitude and longitude of each site is given in the brackets in degrees. The baselines are calculated using Mathematica with the International Terrestrial Reference Frame 2000, rounded to 10 km. All coordinates are consistently extracted from Google Maps [49].

We will quantify in the next section how specific baseline combinations translate into performance and optimization compared to the IDS-NF baseline parameters.

In order to address these purely geometric questions, we consider CERN, FNAL, J-PARC, and RAL as potential host laboratories for the Neutrino Factory.<sup>8</sup> For the potential detector sites, we adopt the conservative point of view that significant rock overburden is needed. This assumptions and the anticipated timescale of the Neutrino Factory limits the choice of potential detector sites to currently investigated, or at least discussed, deep underground laboratories. We list the potential accelerator facilities and underground laboratories together with their locations and baselines between them in Table 2; see Appendix A for more details on the individual locations. The locations of laboratories and detector sites on the

<sup>8</sup>Note that J-PARC is not very far away from KEK, for which the discussion would hardly change.



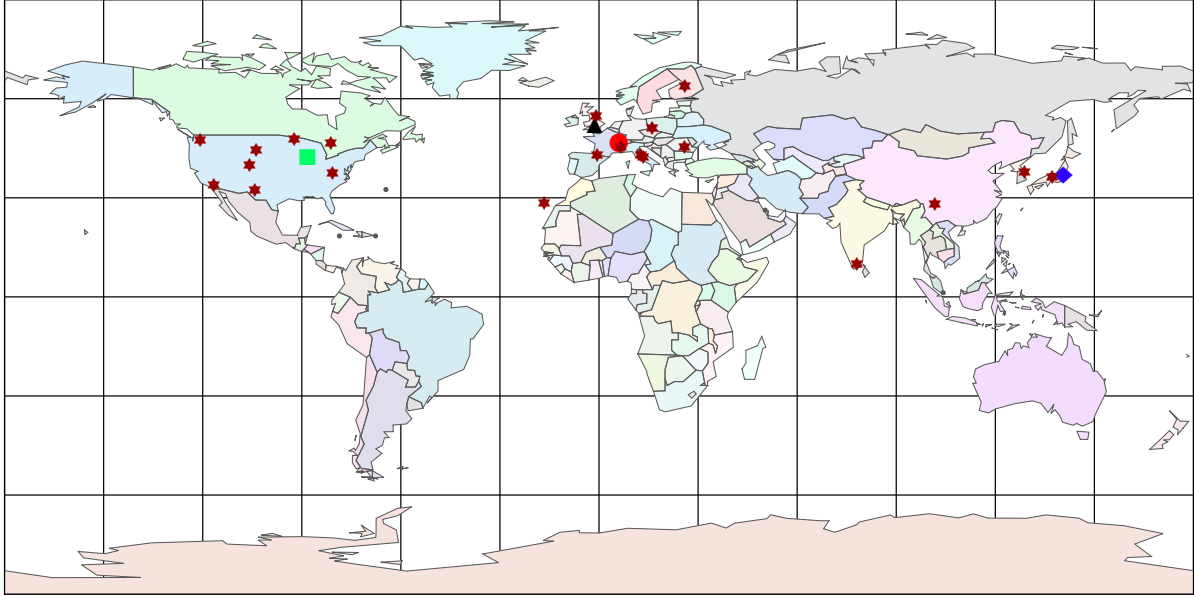


**Figure 7:** A world map including all potential sites of accelerators with large symbols and underground labs with stars.

Earth’s surface can be found in Fig. 7.

For CPV, the IDS-NF baseline has been 3000 km to 5000 km, based on the analysis in Ref. [17]. This conclusion was obtained from the optimization of the  $\theta_{13}$  reach, similar to Fig. 4, left panel. However, from Fig. 5 and Fig. 6 (see also Fig. 8 in Ref. [37]), those shorter baselines are preferable if  $\sin^2 2\theta_{13}$  turns out to be somewhat larger. Therefore, we allow for  $L_1 \in (1500, 5000)$  km for the high energy Neutrino Factory. For degeneracy resolution and the mass hierarchy measurement,  $L_2$  should be close to the “magic baseline” [11] (Fig. 4 is for one specific true value value of  $\delta_{CP}$ ), which can be see, for instance, in Fig. 5 of Ref. [19]. This location does not need to be exact. However, the baseline should not be too short, in order to allow matter effects to pile up and to suppress the CP violating terms, and not too long if too steep active storage rings legs should be avoided. We choose  $L_2 \in (7000, 8000)$  km as a reasonable range, see Ref. [18].

As we can read off from Table 2, there is a very limited number of the short-baseline  $L_1$  detector sites:

**CERN**  $L_1$ : Pyhäsalmi (Finland), Slanic-Prahova (Romania), Gran Canaria (Spain).

**FNAL**  $L_1$ : WIPP, Henderson, Icicle Creek, San Jacinto.

**J-PARC**  $L_1$ : CJPL.

**RAL**  $L_1$ : LNGS (Italy), Pyhäsalmi (Finland), Slanic-Prahova (Romania), Gran Canaria (Spain).

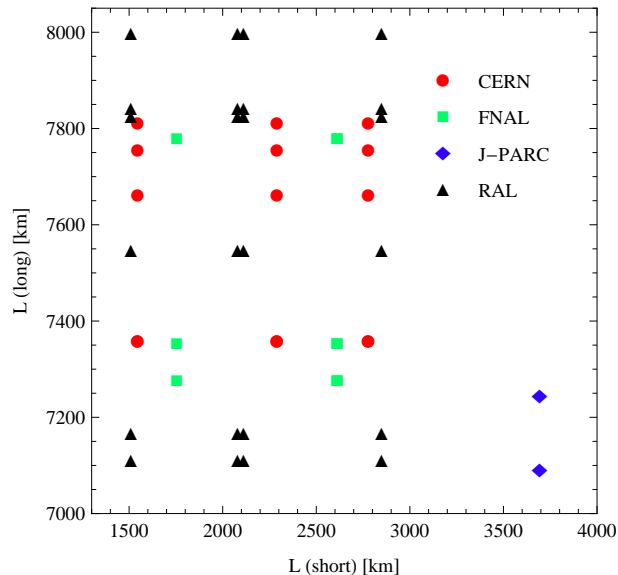


**Figure 8:** Baseline combinations from Table 3 shown in a two baseline plot. The different colors/symbols represent the different laboratories.

We have not found any baseline between 4 000 and 5 000 km. Obviously, we have plenty of options on the second baseline in comparison with the number of the first baseline. It may be noteworthy that CERN-INO and CERN-Homestake are exactly the same distances.

Now with these baseline windows for the short and long baselines, we can, for each laboratory, choose all possible combinations from Table 2. We show these in Fig. 8, with different shapes and colors for each laboratory, and we list them in Table 3. Note that several qualitatively different baseline combinations in Fig. 8 are marked (with the numbers from Table 3), which we will discuss in the next section. In addition to the setups with the above criteria, we have listed one option with FNAL-Homestake as first baseline (#51). As we will demonstrate later, this baseline may be too short for the high energy Neutrino Factory.

Depending on the two baseline combination, it may be possible to use a triangular shaped storage ring instead of two racetracks. Here we follow the discussion in Ref. [10], which the IDS-NF baseline setup with two storage rings is based on. The two racetrack-shaped storage rings are assumed to have a circumference of 1609 m. The active straights are about 600 m long, and, in each storage ring,  $\mu^+$  and  $\mu^-$  circulate in different directions. For a triangular shaped ring, probably two beam lines in the same tunnel are required to store  $\mu^+$  and  $\mu^-$  simultaneously. We assume that the circumference of the triangular ring, representative for the tunneling cost, is the same as for one racetrack, and we assume a (conservative) curvature radius  $R_c$  of about 78 m for the curved sections. For the sake of simplicity, we only consider isosceles triangles with the same useful number of muon decays for the two far detectors. In the racetrack design of the IDS-NF baseline setup,  $2.5 \cdot 10^{20}$  useful muons per year and polarity decay in each straight of each storage ring. For a triangular ring, all muons of one polarity can be injected into the same ring, leading to  $5.0 \cdot 10^{20}$  useful

No.	Lab	Det1	$L_1$	Det2	$L_2$	Straight	Dead	Angle[°]	SF	V-angle[°]
#1	CERN	Pyhäsalmi	2290	CJPL	7660	291	537	135	0.97	44
#2	CERN	Pyhäsalmi	2290	INO	7360	306	507	112	1.02	35
#3	CERN	Pyhäsalmi	2290	Homestake	7360	306	506	111	1.02	35
#4	CERN	Pyhäsalmi	2290	Henderson	7750	308	503	110	1.03	38
#5	CERN	Pyhäsalmi	2290	Icicle Creek	7810	299	520	120	1.00	39
#6	CERN	Slanic	1540	CJPL	7660	286	546	145	0.95	61
#7	CERN	Slanic	1540	INO	7360	284	550	151	0.95	75
#8	CERN	Slanic	1540	Homestake	7360	370	378	61	1.23	47
#9	CERN	Slanic	1540	Henderson	7750	370	378	61	1.23	50
#10	CERN	Slanic	1540	Icicle Creek	7810	354	411	71	1.18	45
#11	CERN	Gran Canaria	2780	CJPL	7660	391	336	51	1.30	77
#12	CERN	Gran Canaria	2780	INO	7360	368	383	63	1.23	52
#13	CERN	Gran Canaria	2780	Homestake	7360	313	493	104	1.04	36
#14	CERN	Gran Canaria	2780	Henderson	7750	311	497	106	1.04	38
#15	CERN	Gran Canaria	2780	Icicle Creek	7810	322	475	95	1.07	39
#16	FNAL	WIPP	1760	LNGS	7350	408	304	44	1.36	80
#17	FNAL	WIPP	1760	Slanic	7780	398	323	48	1.33	72
#18	FNAL	WIPP	1760	Umbria	7280	409	302	43	1.36	80
#19	FNAL	Icicle Creek	2610	LNGS	7350	345	430	77	1.15	42
#20	FNAL	Icicle Creek	2610	Slanic	7780	335	450	84	1.12	42
#21	FNAL	Icicle Creek	2610	Umbria	7280	345	429	77	1.15	42
#22	FNAL	San Jacinto	2610	LNGS	7350	384	352	55	1.28	61
#23	FNAL	San Jacinto	2610	Slanic	7780	371	376	61	1.24	57
#24	FNAL	San Jacinto	2610	Umbria	7280	384	350	54	1.28	61
#25	J-PARC	CJPL	3690	Pyhäsalmi	7090	301	517	118	1.00	34
#26	J-PARC	CJPL	3690	Icicle Creek	7240	364	390	65	1.21	55
#27	RAL	LNGS	1510	CJPL	7840	304	511	114	1.01	39
#28	RAL	LNGS	1510	INO	7820	290	538	136	0.97	50
#29	RAL	LNGS	1510	WIPP	7540	408	302	43	1.36	82
#30	RAL	LNGS	1510	Henderson	7110	415	288	41	1.38	90
#31	RAL	LNGS	1510	Icicle Creek	7160	409	300	43	1.36	73
#32	RAL	LNGS	1510	San Jacinto	8000	403	313	46	1.34	87
#33	RAL	Pyhäsalmi	2080	CJPL	7840	286	546	145	0.95	58
#34	RAL	Pyhäsalmi	2080	INO	7820	296	526	125	0.99	41
#35	RAL	Pyhäsalmi	2080	WIPP	7540	330	460	88	1.10	38
#36	RAL	Pyhäsalmi	2080	Henderson	7110	324	470	93	1.08	35
#37	RAL	Pyhäsalmi	2080	Icicle Creek	7160	312	494	105	1.04	34
#38	RAL	Pyhäsalmi	2080	San Jacinto	8000	321	477	96	1.07	39
#39	RAL	Slanic	2110	CJPL	7840	290	539	137	0.97	48
#40	RAL	Slanic	2110	INO	7820	284	550	151	0.95	79
#41	RAL	Slanic	2110	WIPP	7540	393	333	50	1.31	67
#42	RAL	Slanic	2110	Henderson	7110	392	336	51	1.31	60
#43	RAL	Slanic	2110	Icicle Creek	7160	374	370	59	1.25	50
#44	RAL	Slanic	2110	San Jacinto	8000	380	359	56	1.27	62
#45	RAL	Gran Canaria	2850	CJPL	7840	377	366	58	1.26	63
#46	RAL	Gran Canaria	2850	INO	7820	347	425	75	1.16	46
#47	RAL	Gran Canaria	2850	WIPP	7540	318	483	99	1.06	37
#48	RAL	Gran Canaria	2850	Henderson	7110	323	472	94	1.08	36
#49	RAL	Gran Canaria	2850	Icicle Creek	7160	337	444	82	1.12	40
#50	RAL	Gran Canaria	2850	San Jacinto	8000	325	469	92	1.08	41
#51	FNAL	Homestake	1290	LNGS	7350	359	400	68	1.20	42

**Table 3:** Considered two-baseline combinations (see main text). The five right columns give the parameters of an isosceles triangle as storage ring: straight length (meters), dead length (meters), apex angle (degrees), scale factor SF (compared to two racetracks), angle to vertical (degrees).

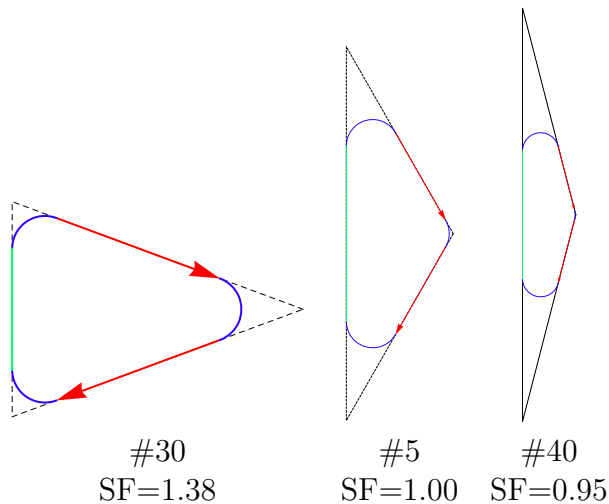


**Figure 9:** Examples for three isosceles triangular-shaped rings (maximum efficiency, racetrack-like efficiency, and minimum efficiency, respectively). The numbers refer to Table 3.

muon decays per year and polarity over a straight length of 600 m, which corresponds to  $SF=2$ . Of course, due to the fixed circumference, the straights will be shorter than 600 m for the triangle, *i.e.*,  $SF < 2$ . Note that  $SF=1$  corresponds to the same luminosity of the two designs. Obviously, if  $SF > 1$ , the triangle is more efficient, possibly with a factor of two lower tunneling cost (because only one tunnel is needed). If  $SF \lesssim 1$ , the loss of efficiency could be compensated by a slightly larger storage ring. For  $SF \lesssim 0.5$ , the two racetracks are definitively the better option. Note that synchrotron losses in the curved sections of the storage rings and other beam losses are taken into account for the racetrack-shaped geometry, yielding the anticipated number of useful muon decays for the IDS-NF baseline. We do not expect that these losses change drastically for a triangular-shaped ring. For example, for the curved sections, we have assumed the same curvature radius, and the three curves sections add up to a circle just as for the two curves sections of a racetrack-shaped ring. Since the circumference of the triangular and racetrack shaped rings is the same, the muons are exposed to the same curved section distance over their lifetime.

As the first observation, a triangular shaped ring can always be built if the circumference of the ring is larger than  $2\pi R_c$  ( $R_c$ : curvature radius curved section), which we have satisfied. This can be easily seen by the fact that in the smallest (extreme) case, the triangle with curved sections will collapse into a circle (with zero straight lengths). For larger triangles, the efficiency of the active legs ( $SF$ ) may still be extremely small. However, we list in Table 3 the triangular geometry in terms of straight lengths, dead section length, apex angle,  $SF$ , and V-angle (angle between triangle plane and vertical), and it turns out that  $0.95 \lesssim SF \lesssim 1.38$ . In the optimal case (#30), the V-angle is  $90^\circ$ . This means that a triangle could be built for all of the considered options. We show three examples for maximum efficiency, racetrack-like efficiency, and minimum efficiency, respectively, in Fig. 9, where also the numbers from Table 3 are given. In the extreme cases, the triangle resembles a racetrack with either a very short or very long dead section. In the worst case, if the two detector locations are quite aligned, less than 50% of the useful muon decays over the whole ring can be used. However, the factor of two higher muon injection rate compensates for that.

In this discussion we have ignored how deep the tunnels would be and that two racetracks have other advantages. For instance, if one racetrack or one detector needs maintenance, all muons can be injected into the other storage ring without loss of performance integrated over the whole operation time. However, this discussion is interesting from a different perspective: Earlier in Sec. 2.3, we have shown that a single baseline operation may be more beneficial in parts of the parameter space, where one of the reasons is a factor of two gain in exposure compared to the operation of two racetracks. However, if a triangular ring is built, the argument changes. In Fig. 3, the 100kt+50kt option has an exposure of  $150 \text{ kt} \cdot 1$  (SF)=150 kt and the 100kt option an exposure of  $100 \text{ kt} \cdot 2$  (SF)=200 kt. For the triangle, one in the most optimistic case for the 100kt+50kt option has an exposure of  $150 \text{ kt} \cdot 1.38$  (SF) $\simeq$ 200 kt, which is the same as for the one baseline case – at a much better sensitivity, and with the same storage ring circumference. From a different point of view, one has the performance depicted by 100kt+50kt in Fig. 3 in that case already with two 72 kt and 36 kt detectors. Thus, for small  $\sin^2 2\theta_{13}$  and proper detector sites, the triangle may finally be the better choice. Note that in the following, unless noted otherwise, we do not use the SF from Table 3, but use SF=1 instead (two racetracks).

In summary, we have demonstrated that reasonable pairs of detector locations can be found for the considered accelerator laboratories. We have stated that one could always use a triangular-shaped storage ring with a similar efficiency as two racetracks from purely geometrical arguments, and that the efficiency varies at about 40% among the different options.

## 5 Site-specific performance and energy optimization

Here we discuss the performance of site-specific setups, as well as the optimization of  $E_\mu$  for specific sites. Because of the large number of options considered, we only show examples in this section, whereas the plots for all discussed sites can be found in Appendix B.

Let us first of all quantify the performance in comparison to the IDS-NF baseline combination 4 000 km+7 500 km at SF=1. Therefore, we show in Fig. 10 the discovery reach for CPV, MH, and  $\theta_{13}$  discovery ( $3\sigma$ ) for a number of qualitatively different selected baseline combinations for different accelerator laboratories (in rows). For each laboratory, we have chosen an example roughly representing the best case and an example close to the worst case for the chosen  $E_\mu = 25 \text{ GeV}$ , as well as we show the IDS reference values. Here two racetrack-shaped storage rings (SF=1) are assumed. In all accelerator cases for CPV, options can be found which perform better than the IDS combination if  $\sin^2 2\theta_{13} \gtrsim 10^{-2}$ , because large values of  $\sin^2 2\theta_{13}$  prefer shorter CPV baselines, as discussed earlier. In these cases, even a single baseline option with a lower  $E_\mu$  could be preferable. For  $10^{-3} \lesssim \sin^2 2\theta_{13} \lesssim 10^{-2}$ , options close to the IDS performance can be easily identified. For  $\sin^2 2\theta_{13} \ll 10^{-3}$ , the IDS combination can roughly be matched, but the sensitivity cannot be exceeded, at least not with the racetrack-shaped storage rings. The reason is that we do not use any baselines close to, or exceeding 4 000 km. Because of the absence of potential detector sites, one may want to study either alternative locations, or the possibility to use MIND close to the surface. In this case, the long baseline may actually help for background suppression, since neutrinos

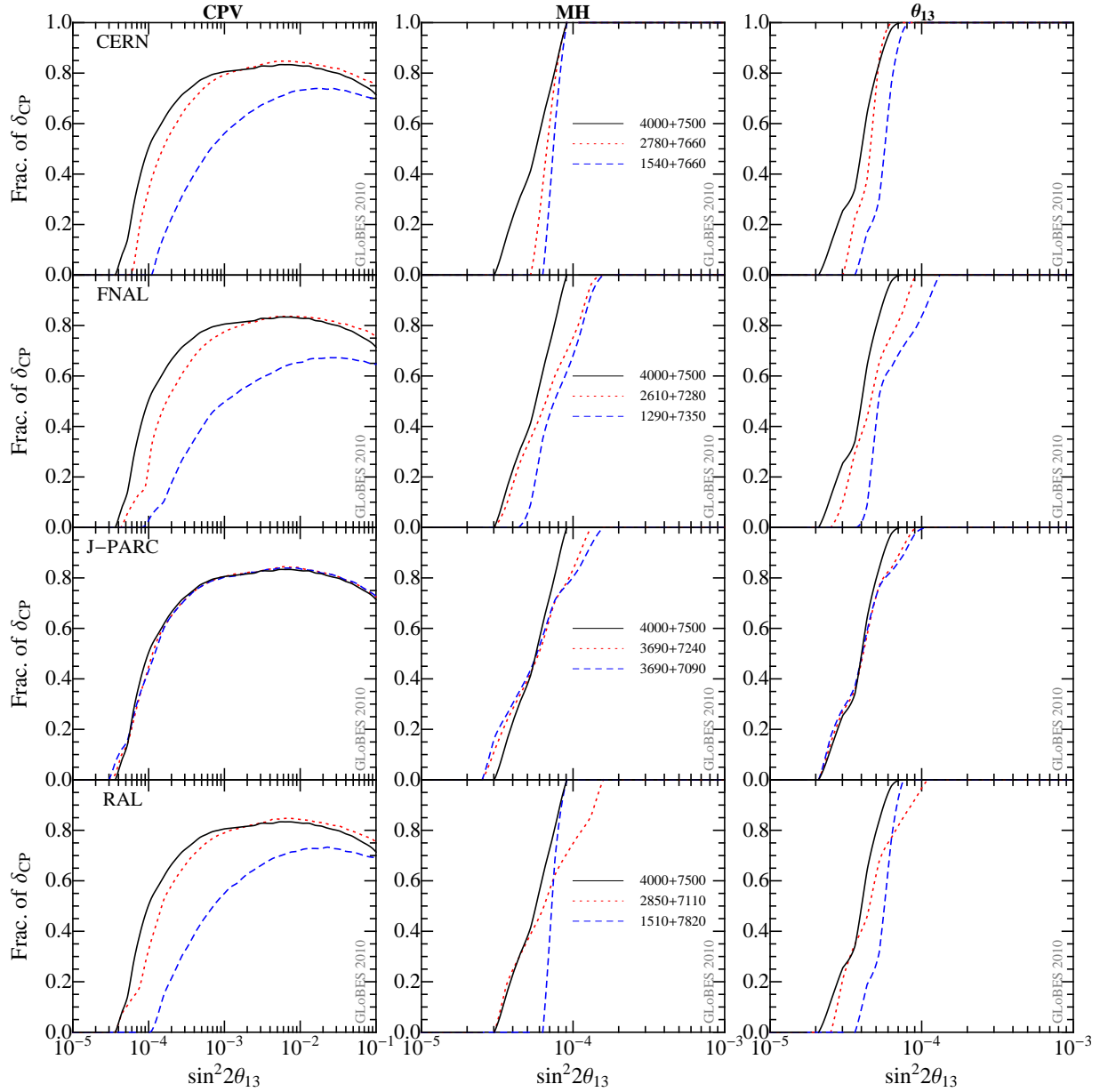


**Figure 10:** The discovery reach of CPV, MH, and  $\theta_{13}$  ( $3\sigma$ , in columns) for selected baseline combinations for different accelerator laboratories (in rows). In all panels, the curves for the IDS reference combination 4 000 km+7 500 km with new-NF is shown for reference. Here  $E_\mu$  is fixed to 25 GeV with two 50 kt detectors, and SF=1 is used in all cases (two racetrack-shaped storage rings).

from directions close to the beam have to travel through a significant amount of rock then. In the worst case scenarios, significant sensitivity losses may have to be taken into account, especially if not long enough CPV baselines are used. The MH discovery, on the other hand, is driven by the long baseline, but also benefits from a longer short baseline. For the optimal options, the IDS sensitivity can be matched, although it may be a bit different as a function of  $\delta_{\text{CP}}$ . Similar results are obtained for the  $\theta_{13}$  discovery reach.

In Appendix B, we show the performances of the discussed combinations (#1 to #50) from Table 3. In each case, we compare the performances with racetracks (SF=1, dotted curves), triangular-shaped geometry (SF from Table 3, dashed curves), and IDS combination (SF=1, solid curves). Here we just mention some of the most interesting options from these figures, especially those with excellent sensitivity for  $\sin^2 2\theta_{13} \lesssim 10^{-2}$  which can be further improved by a triangular shaped ring. Here CERN or RAL to Gran Canaria and to CJPL or INO are interesting options with a significant sensitivity gain and good absolute performance. In addition, J-PARC to CJPL and Iceberg is, in fact, the only option we find which can exceed the IDS reference performance for small  $\sin^2 2\theta_{13}$ . For options with shorter baselines, the performance also improves significantly in many cases by using a triangular geometry, but that cannot compensate for the baseline choice. In no case, the performance is significantly worse using a triangle.

Another interesting question is the optimization of  $E_\mu$  for specific two baseline setups. Remember that the two baseline Neutrino Factory is mostly relevant for small  $\sin^2 2\theta_{13}$ . Here we choose the combinations from RAL as example, see Fig. 11, the other laboratories are shown in Appendix B. Basically, we can identify three different sets of curves in that figure, which correspond to the three different CPV baselines in Table 3: (a)  $L_1 = 1510$  km, (b)  $L_1 \simeq 2100$  km (two different ones), (c)  $L_1 = 2848$  km. Depending on the value of  $\sin^2 2\theta_{13}$  and  $E_\mu$ , one of these three sets performs best: below about 7-8 GeV (depending on  $\sin^2 2\theta_{13}$ ), (a) is best, between about 8 and 12 GeV (b) is best, and above 10-14 GeV, (c) is best. This results more or less reproduces the green-field optimization. Note that for  $\sin^2 2\theta_{13} \lesssim 10^{-2}$ , the case for which the two baseline Neutrino Factory is the relevant choice, the long CPV baseline options are better in terms of absolute performance, provided that  $E_\mu$  is high enough. In addition, note that the IDS reference prefers  $E_\mu \gtrsim 20$  GeV in all cases, where the discovery reaches saturate. To summarize, the optimal muon energy does not only depend on  $\sin^2 2\theta_{13}$ , but also on the specific two baseline combination. However, in many cases, the performance saturates at about 12-15 GeV (see, *e.g.*,  $\sin^2 2\theta_{13} = 10^{-4}$ ), and in some cases may even decrease for too high  $E_\mu$ . The IDS-NF baseline choice  $E_\mu = 25$  GeV can be understood as an aggressive option from the current point of view. However, note that for any given baseline combination, the optimization of  $E_\mu$  can be easily performed. From the machine point of view, it should be easy to “down-grade” the setup then.

## 6 Summary and conclusions

In this study, we have revisited the optimization of the Neutrino Factory based on the most up-to-date analysis of the MIND detector using migration matrices. We have also considered possible backgrounds from taus, which come from  $\nu_\tau$  charged current interactions

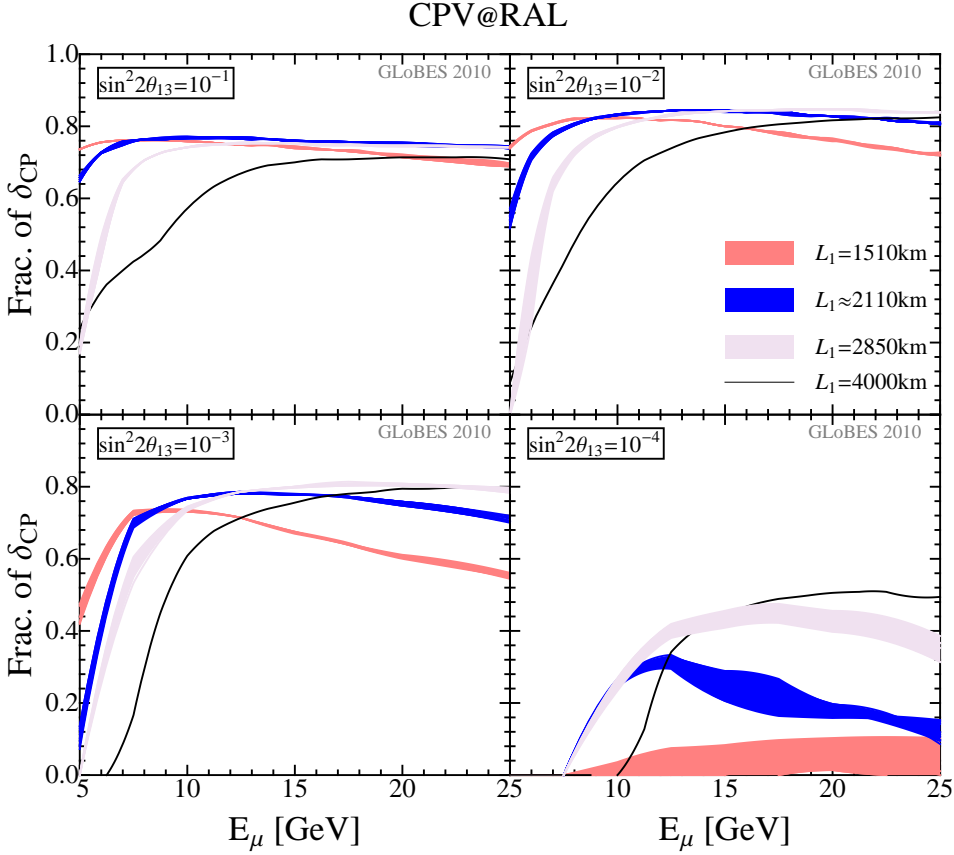


**Figure 11:** CPV discovery reach at RAL as a function of  $E_\mu$  for all RAL-options in Table 3 at the  $3\sigma$  CL for different values of (true)  $\sin^2 2\theta_{13}$  (as given in the panels). Here we assume SF=1.0 and two 50 kt detectors. We group the different baseline combinations according to the shorter baseline  $L_1$ , as shown in the legend. The bands basically reflect the variation of the second baseline. The IDS-NF baseline combination is shown by the black curves with  $L_1 = 4000$  km and  $L_2 = 7500$  km.

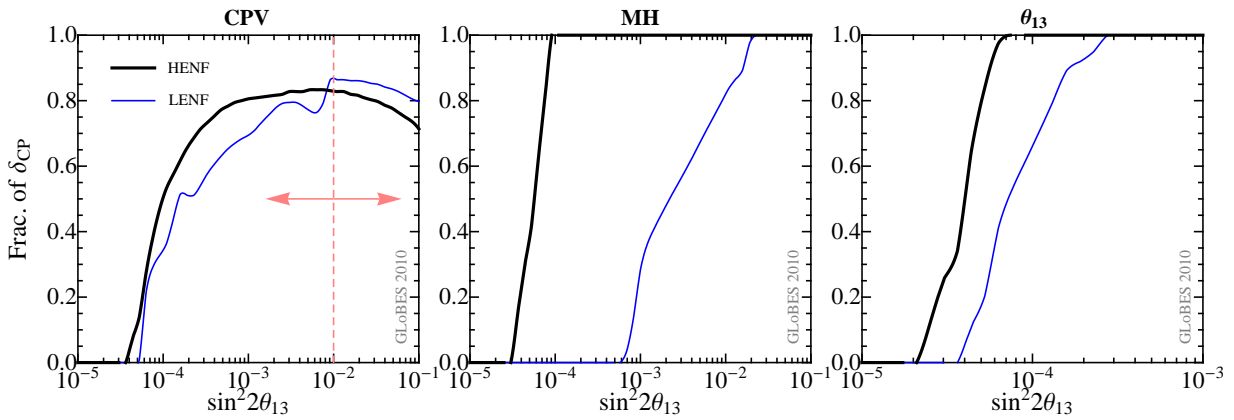


**Figure 12:** A comparison of the discovery reaches of CPV, MH, and  $\theta_{13}$  at the  $3\sigma$  CL between a low energy single baseline neutrino factory (LENF) with  $E_\mu = 10$  GeV and  $L = 2000$  km (*cf.*, Fig. 5, upper left panel), and a high energy two baseline neutrino factory (HENF) with  $E_\mu = 25$  GeV,  $L_1 = 4000$  km, and  $L_2 = 7500$  km (*cf.*, Fig. 6, lower right panel).



in the detector, and which practically cannot be distinguished from muons. We have found that the resulting backgrounds do not have a visible impact on the CPV, MH, and  $\theta_{13}$  discovery reaches. A more refined discussion will require, however, a consistent treatment of all migration matrices.

Although the optimization of the Neutrino Factory does generically not change with the new detector simulation, there are a number of interesting observations. The lower threshold and higher efficiencies compared to earlier simulations imply that the MIND detector characteristics are getting more similar to the characteristics of the detectors proposed for the low energy Neutrino Factory (*e.g.*, a magnetized T ASD). We could demonstrate that we recover the  $L$ - $E_\mu$ -optimization of the low energy Neutrino Factory for large  $\sin^2 2\theta_{13}$ : In this case, a single baseline Neutrino Factory with  $E_\mu$  as low as 5 GeV and a baseline as short as FNAL-Homestake (about 1 300 km) might be sufficient. For small  $\sin^2 2\theta_{13} < 10^{-2}$ , however, we find that a two baseline Neutrino Factory with one baseline between about 2 500 km and 5 000 km, the other one at about the magic baseline 7 500 km is ideal. This recovers the results from Ref. [17]. We summarize this in Fig. 12, where we compare the performance of the optimal single baseline low energy Neutrino Factory with the optimal two baseline high energy Neutrino Factory for the same MIND detector. One can clearly see that for  $\sin^2 2\theta_{13} \gtrsim 10^{-2}$  the low energy version can perform all of the required measurements, whereas for smaller values the high energy Neutrino Factory is clearly better. This means that this different optimization would be sufficient to compensate for the relative deterioration of performance at large  $\sin^2 2\theta_{13}$  observed in the traditional high-energy Neutrino Factory. If  $\sin^2 2\theta_{13}$  was known, the shorter (CPV) baseline could even be optimized: The larger  $\sin^2 2\theta_{13}$  was, the shorter CPV baselines would be preferred in the mentioned baseline window. The next generation of experiments will tell us if  $\sin^2 2\theta_{13} \gtrsim 10^{-2}$  or smaller, see, *e.g.*, Ref. [50], therefore, we can optimize for the large  $\sin^2 2\theta_{13} > 0.01$  case. Note that a more refined optimization depending on the size of  $\sin^2 2\theta_{13}$  may be possible for a staged Neutrino Factory approach, as it is illustrated in Ref. [37].

Apart from the optimization of the green-field Neutrino Factory, we have performed a site-specific analysis for the high energy Neutrino Factory, assuming that it requires two baselines. We have considered four different accelerator laboratories on three different continents (CERN, FNAL, J-PARC, RAL) and a number of potential detector locations in suggested underground laboratories. We have found that in all cases plausible baseline combinations can be found. However, for small  $\sin^2 2\theta_{13}$ , where a baseline between 2 500 and 5 000 km is preferred for CPV, we only found one possible baseline: J-PARC to CJPL (China). Therefore, we propose that possible underground sites for this baseline window should be investigated. In addition, we propose to study the MIND performance on the surface, since surface operation would greatly facilitate site and baseline selection.

We have also investigated the possibility to use a triangular-shaped muon storage ring compared to two racetracks, where the efficiency is a function of the Earth geometry and the chosen source and detector locations. We have first of all shown that solely based on geometry a triangular ring could be used in either case, without significant loss of luminosity. Then we have identified a number of baseline combinations with reasonable baseline lengths for which the triangle would be especially interesting: CERN or RAL to Gran Canaria and to CJPL or INO. In addition, J-PARC to CJPL and Iceberg is, in fact, the only option

we found which can exceed the IDS reference performance for small  $\sin^2 2\theta_{13}$ . We have also pointed out that using a triangular-shaped ring, the decision between one and two baselines does not emerge, and that, from the physics point of view, the two baseline combination is more efficient for the same exposure.

As far as the optimization  $E_\mu$  is concerned, the feature of the new detector simulation that the backgrounds are typically reconstructed at lower energies and that the threshold is lower leads to new insights. Especially for the high energy Neutrino Factory in the context of specific baseline combinations, the CPV performance in some cases saturates at lower muon energies than 25 GeV. Although the current IDS-NF baseline setup with  $E_\mu = 25$  GeV is still optimal for the optimal baseline combination, and high  $E_\mu$  typically do not harm for small  $\sin^2 2\theta_{13}$ , smaller energies may be preferred for specific sites.

We conclude that the low energy and high energy Neutrino Factory should not be regarded as separate options. Let us emphasize that the optimization, for instance, of  $E_\mu$  is a function of  $\sin^2 2\theta_{13}$ , the detector response, and the specific sites chosen for detector and accelerators. Therefore, the IDS-NF baseline with  $E_\mu = 25$  GeV should be understood as most conservative choice, which can be downgraded in specific scenarios/for specific detectors. From the machine point of view, we recommend to choose splitting points between the different accelerator components at about 5 and 12 GeV, which will allow for  $E_\mu = 5, 12, \text{ or } 25$  GeV. The final choice has to be made based on the knowledge on  $\sin^2 2\theta_{13}$  at the time of decision, the choice of the detector, and the specific site.

## Acknowledgments

We thank Alain Blondel, Anselmo Cervera, Pilar Coloma, Andrea Donini, and Paul Soler for insightful discussions and thank Andrew Liang and Davide Meloni for providing the latest data files of the migration matrices. JT is also indebted to Xiaobo Huang for help with the usage of ROOT.

This work has been supported by the Emmy Noether program of Deutsche Forschungsgemeinschaft (DFG), contract no. WI 2639/2-1 [J.T, W.W.], by the DFG-funded research training group 1147 ‘‘Theoretical astrophysics and particle physics’’ [J.T.], and by the European Union under the European Commission Framework Programme 07 Design Study EUROnu, Project 212372. This work has also been supported by the U.S. Department of Energy under award number DE-SC0003915. S.K.A acknowledges in addition the support from the project Consolider-Ingenio CUP.

## A Locations of accelerator facilities and underground laboratories

We use Google Maps [49] to find the exact locations (latitudes and longitudes) of considered accelerator facilities and underground laboratories. In the following, we provide the details of the locations based on which the latitudes and longitudes have been obtained.

## A.1 Accelerator facilities

- CERN

Latitude :  $46.24^\circ$  N & Longitude :  $6.05^\circ$  E

Route de Meyrin 385, 1217 Geneve, Schweiz, Switzerland.

- FNAL

Latitude :  $41.85^\circ$  N & Longitude :  $88.28^\circ$  W

Center for Particle Astrophysics, Fermi National Accelerator Laboratory, P.O. Box 500, Kirk Road and Pine Street, Batavia, Illinois 60510-0500 USA.

- J-PARC

Latitude :  $36.47^\circ$  N & Longitude :  $140.57^\circ$  E

Tokai Village, Naka District, Ibaraki Prefecture, Japan.

- RAL

Latitude :  $51.57^\circ$  N & Longitude :  $1.32^\circ$  W

Rutherford Appleton Laboratory, Harwell Science & Innovation Campus, Didcot OX110QX, UK.

## A.2 Underground facilities in USA

- Soudan

Latitude :  $47.82^\circ$  N & Longitude :  $92.24^\circ$  W

Soudan Underground Lab, 30 1st Avenue, Soudan, MN 55782.

- WIPP

Latitude :  $32.37^\circ$  N & Longitude :  $104.23^\circ$  W

The WIPP Experience Exhibit, U.S. Department of Energy, 4021 National Parks Highway, Carlsbad, New Mexico.

- Homestake

Latitude :  $44.35^\circ$  N & Longitude :  $103.77^\circ$  W

Homestake Visitor Center, 160 West Main Street, Lead, SD 57754-1362.

- SNOLAB

Latitude :  $46.47^\circ$  N & Longitude :  $81.19^\circ$  W

SNOLAB, Greater Sudbury, Ontario, Canada.

- Henderson

Latitude :  $39.77^\circ$  N & Longitude :  $105.86^\circ$  W

Henderson Mine and Mill, 1746 County Road 202 Empire, CO 80438.

- Icicle Creek  
Latitude : 47.56° N & Longitude : 120.78° W  
Bridge Creek Campground, Leavenworth, Washington 98826.
- San Jacinto  
Latitude : 33.86° N & Longitude : 116.56° W  
Mt San Jacinto State Park, 1 Tramway Road, Palm Springs, CA 92262-1827.
- Kimballton  
Latitude : 37.37° N & Longitude : 80.67° W  
Kimballton, VA 24136.

### A.3 Underground facilities in Europe

- LNGS  
Latitude : 42.37° N & Longitude : 13.44° E  
Istituto Nazionale Di Fisica Nucleare - Laboratori Nazionali Del Gran Sasso-Ufficio Amministrativo, Strada Statale 17 Bis, L'Aquila, AQ 67100, Italy.
- Pyhäsalmi  
Latitude : 63.68° N & Longitude : 25.98° E  
86800 Pyhajarvi municipality in the south of Oulu province, Finland.
- Slanic  
Latitude : 45.27° N & Longitude : 25.95° E  
Largest Salt mine in Europe, Prahova, Slanic, Romania.
- Boulby  
Latitude : 54.56° N & Longitude : 0.81° W  
Boulby Potash Mine located just southeast of the village of Boulby, on the northeast coast of the North Yorkshire Moors in Redcar and Cleveland, England.
- Canfranc  
Latitude : 42.76° N & Longitude : 0.51° W  
Laboratorio Subterráneo de Canfranc lies physically between New Road tunnel and Old Railway tunnel of Canfranc, Spain.
- Fréjus  
Latitude : 45.20° N & Longitude : 6.67° E  
Laboratoire souterrain de Modane, Carre Sciences, 73500 Modane, France.

- SUNLAB  
Latitude : 51.22° N & Longitude : 16.16° E  
Polkowice-Sieroszowice mine near Wroclaw in Poland.
- Umbria  
Latitude : 42.98° N & Longitude : 12.64° E  
Umbria, IT in Italy.
- Gran Canaria  
Latitude : 28.39° N & Longitude : 16.59° W  
Gran Canaria in Spain.

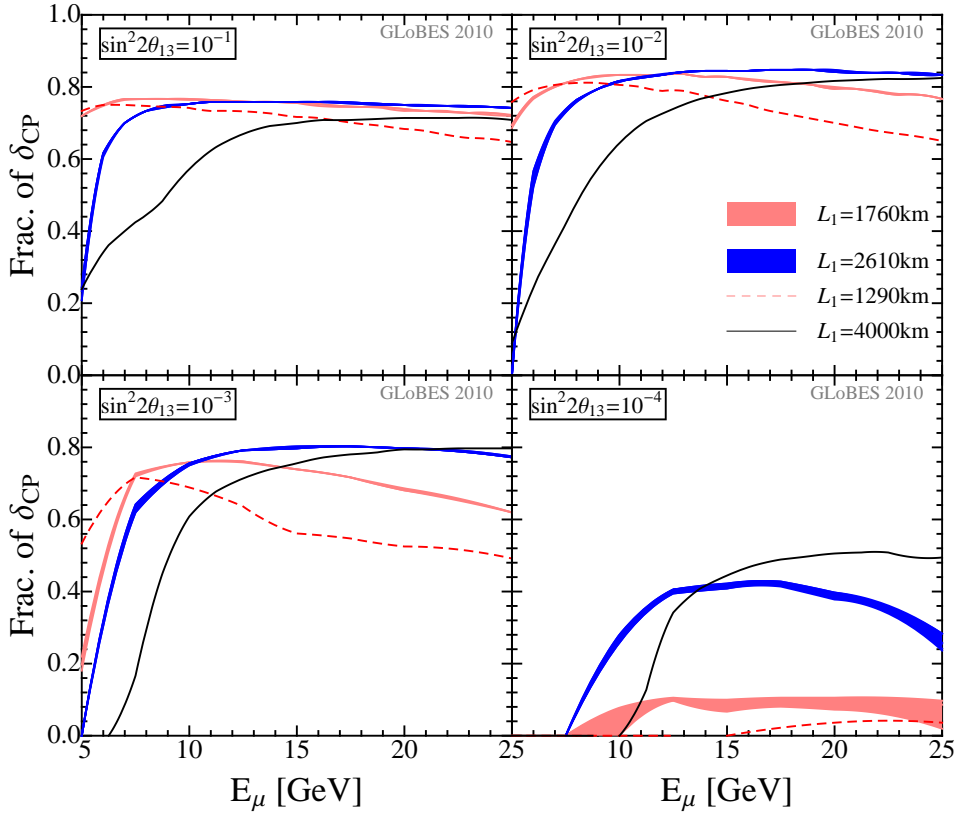
#### A.4 Underground facilities in Asia

- CJPL  
Latitude : 28.15° N & Longitude : 101.71° E  
China JinPing Deep Underground Laboratory at Sichuan Province in China close to Jinping mountain.
- Kamioka  
Latitude : 36.14° N & Longitude : 137.24° E  
Kamioka is located underground in the Mozumi Mine of the Kamioka Mining and Smelting Co. near the Kamioka section of the city of Hida in Gifu Prefecture, Japan.
- YangYang  
Latitude : 37.77° N & Longitude : 128.89° E  
YangYang underground laboratory (Y2L) is located at a depth of 700 m under an earth overburden in South Korea.
- INO  
Latitude : 9.92° N & Longitude : 78.12° E  
Bodi West Hills Reserved Forest in Theni district of Tamil Nadu, India.

## B Details for all considered two-baseline combinations

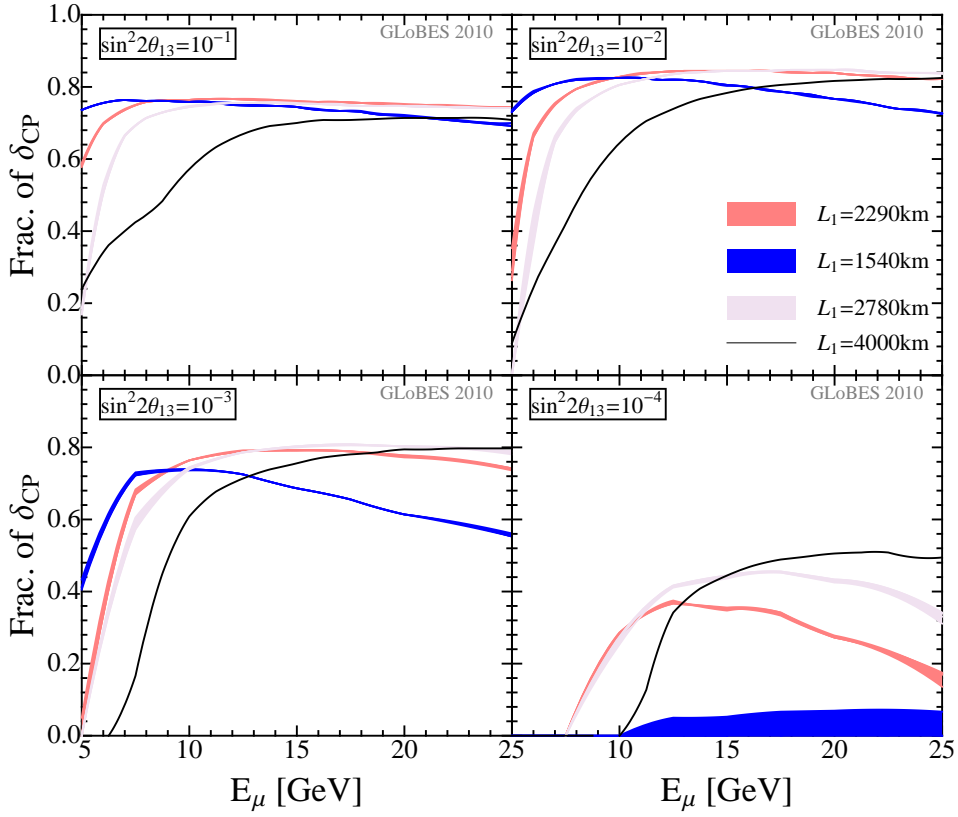
Here we first of all show the figures similar to Fig. 11 for the different accelerator laboratories for the sake of completeness: Fig. 13, Fig. 14, and Fig. 15. Although there are quantitative differences, there are no qualitatively new insights, apart from Fig. 13. Here the FNAL-Homestake option is shown separately, which indeed peaks at even lower  $E_\mu \simeq 5 \text{ GeV}$  for large  $\sin^2 2\theta_{13}$ .

### CPV@FNAL

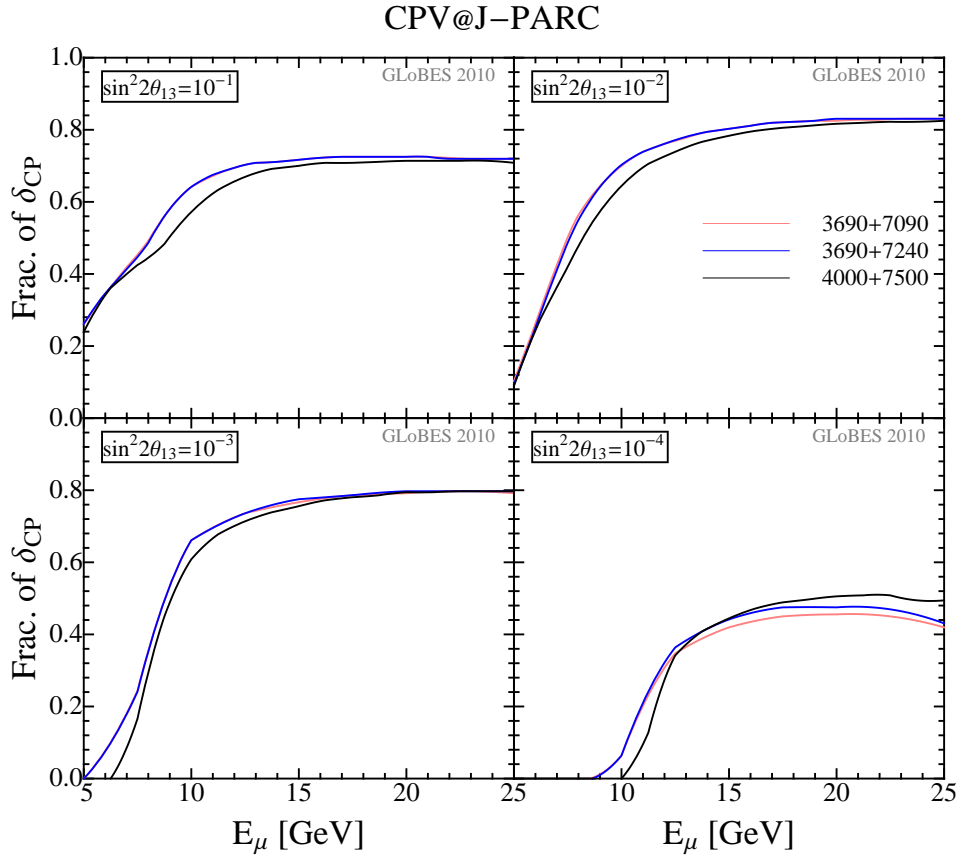


**Figure 13:** CPV discovery reach at FNAL as a function of  $E_\mu$  for all FNAL-options in Table 3 at the  $3\sigma$  CL for different values of (true)  $\sin^2 2\theta_{13}$  (as given in the panels). Here we assume  $SF=1.0$  and two 50 kt detectors. We group the different baseline combinations according to the shorter baseline  $L_1$ , as shown in the legend. The bands basically reflect the variation of the second baseline. The IDS-NF baseline combination is shown by the black curves with  $L_1 = 4000$  km and  $L_2 = 7500$  km.

### CPV@CERN

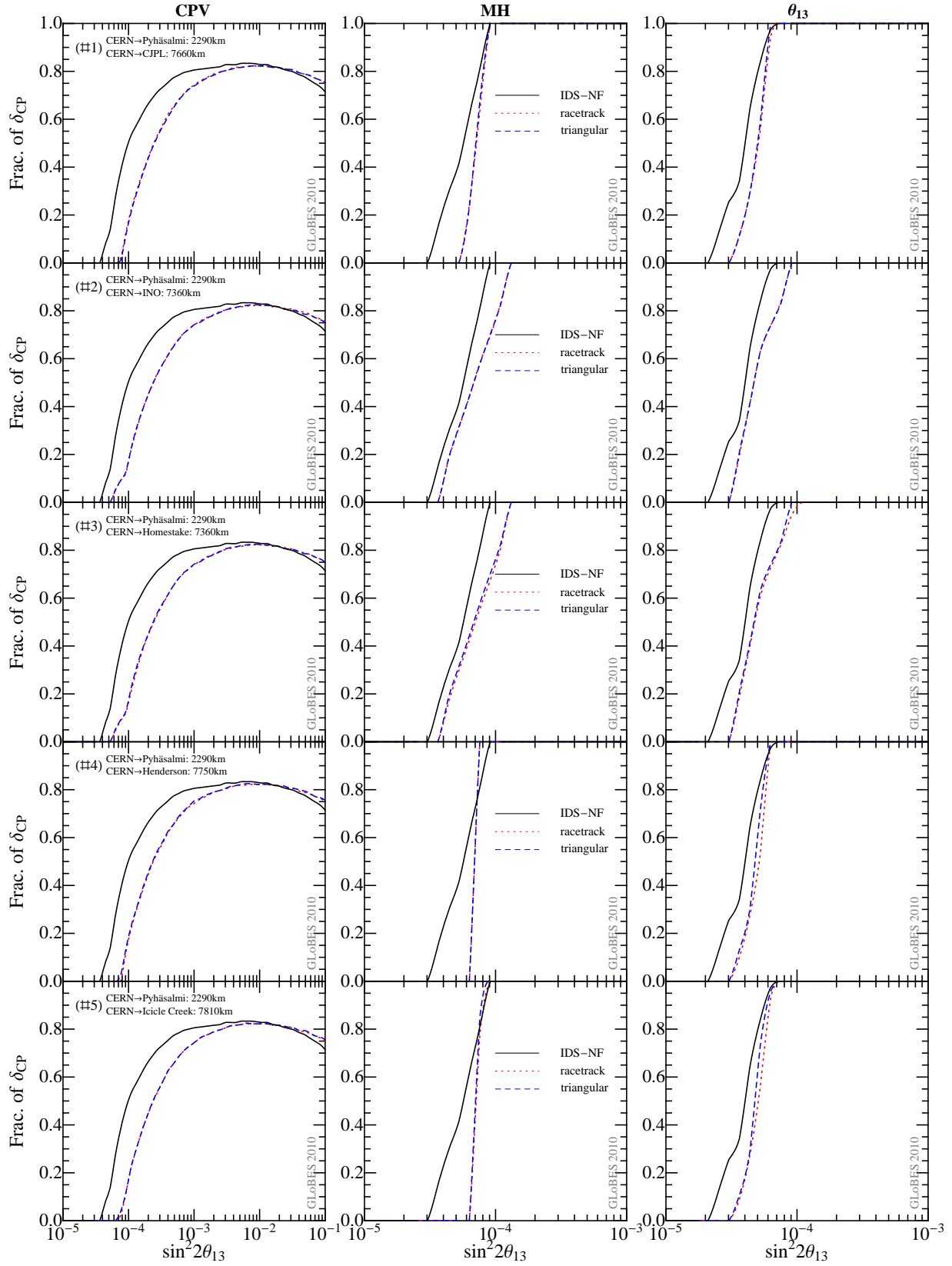


**Figure 14:** CPV discovery reach at CERN as a function of  $E_\mu$  for all CERN-options in Table 3 at the  $3\sigma$  CL for different values of (true)  $\sin^2 2\theta_{13}$  (as given in the panels). Here we assume  $SF=1.0$  and two 50 kt detectors. We group the different baseline combinations according to the shorter baseline  $L_1$ , as shown in the legend. The bands basically reflect the variation of the second baseline. The IDS-NF baseline combination is shown by the black curves with  $L_1 = 4000$  km and  $L_2 = 7500$  km.

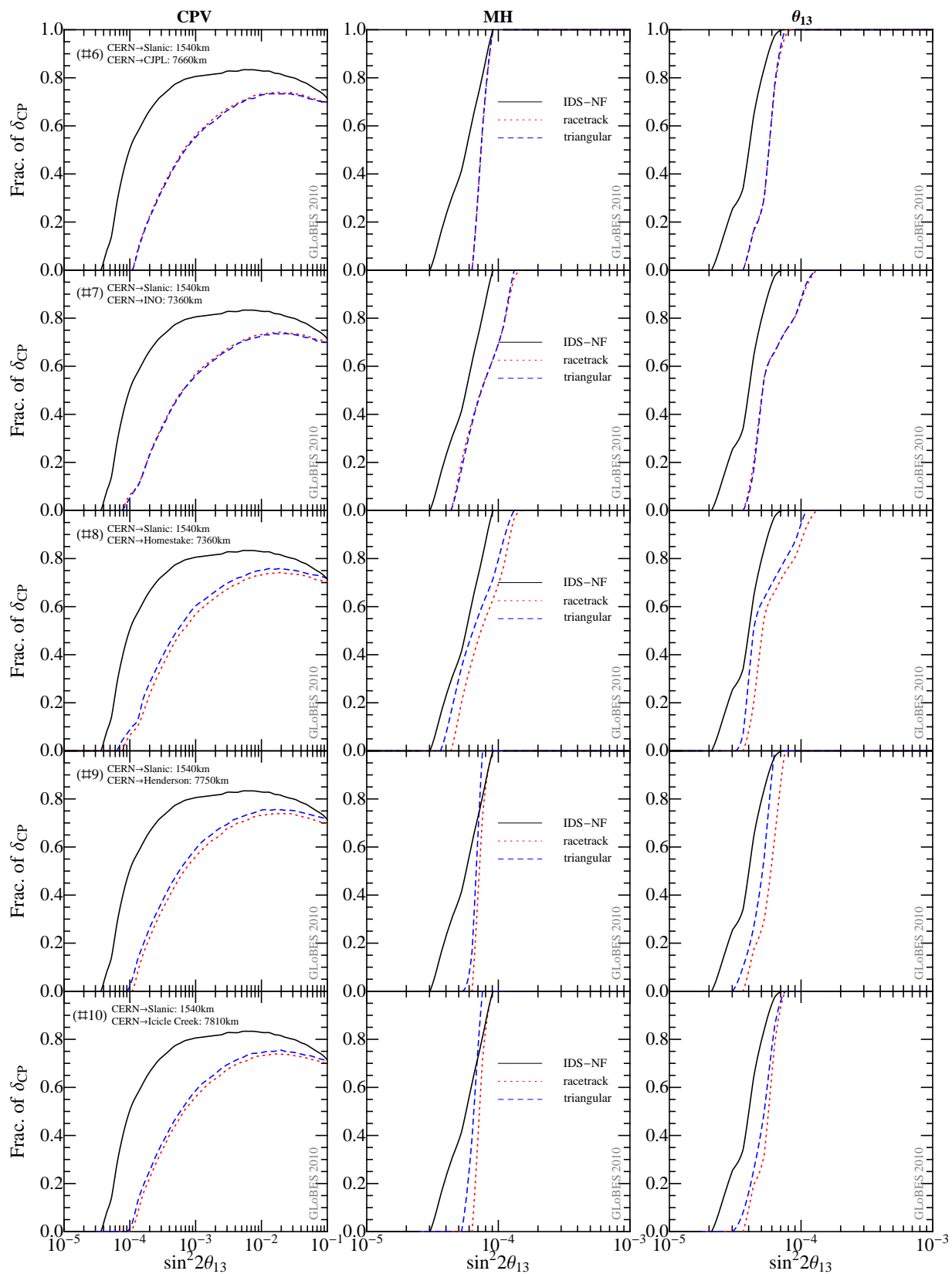


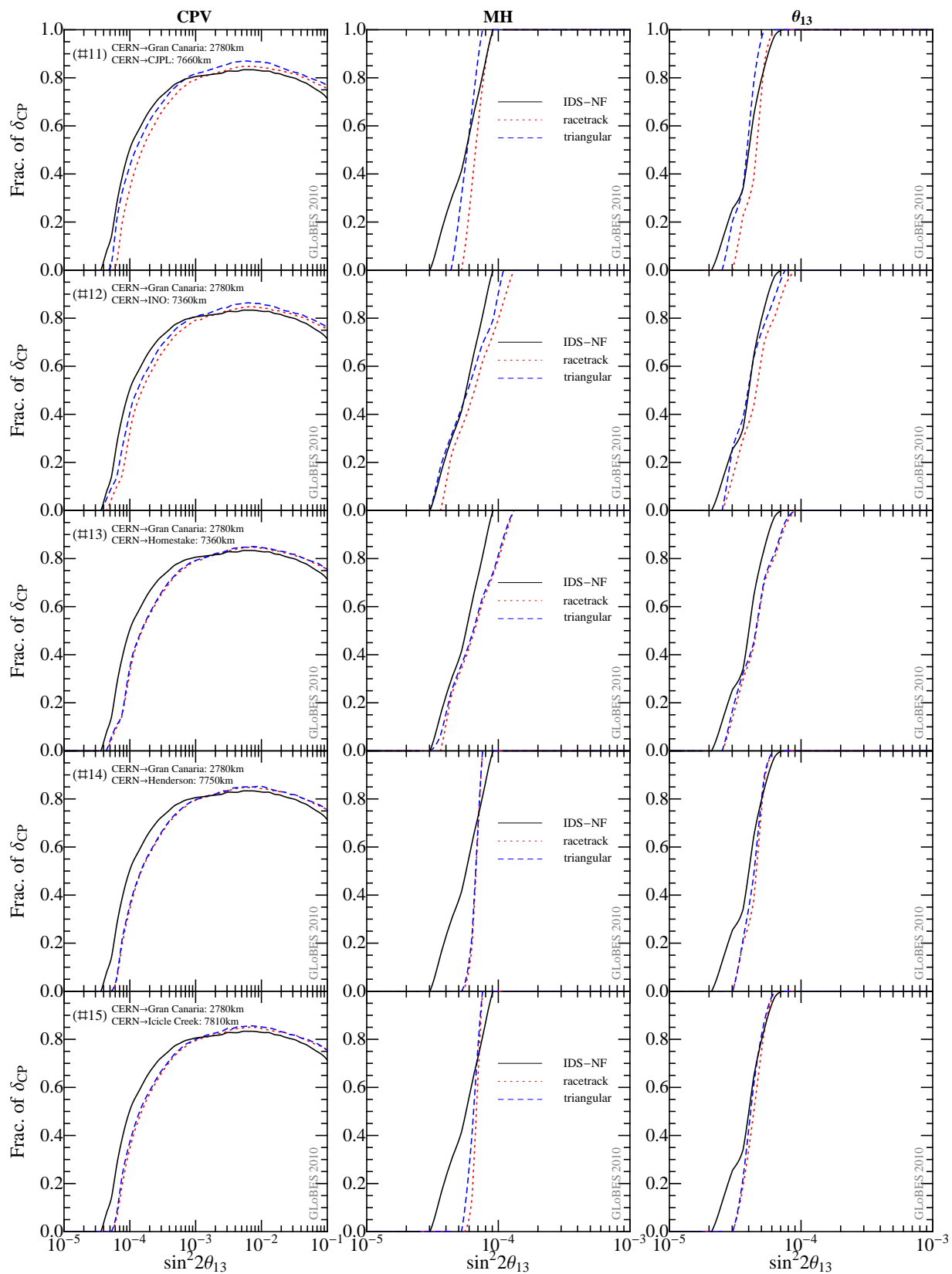
**Figure 15:** CPV discovery reach at J-PARC as a function of  $E_\mu$  for all J-PARC-options in Table 3 at the  $3\sigma$  CL for different values of (true)  $\sin^2 2\theta_{13}$  (as given in the panels). Here we assume SF=1.0 and two 50 kt detectors. The IDS-NF baseline combination is shown by the black curves with  $L_1 = 4000$  km and  $L_2 = 7500$  km.

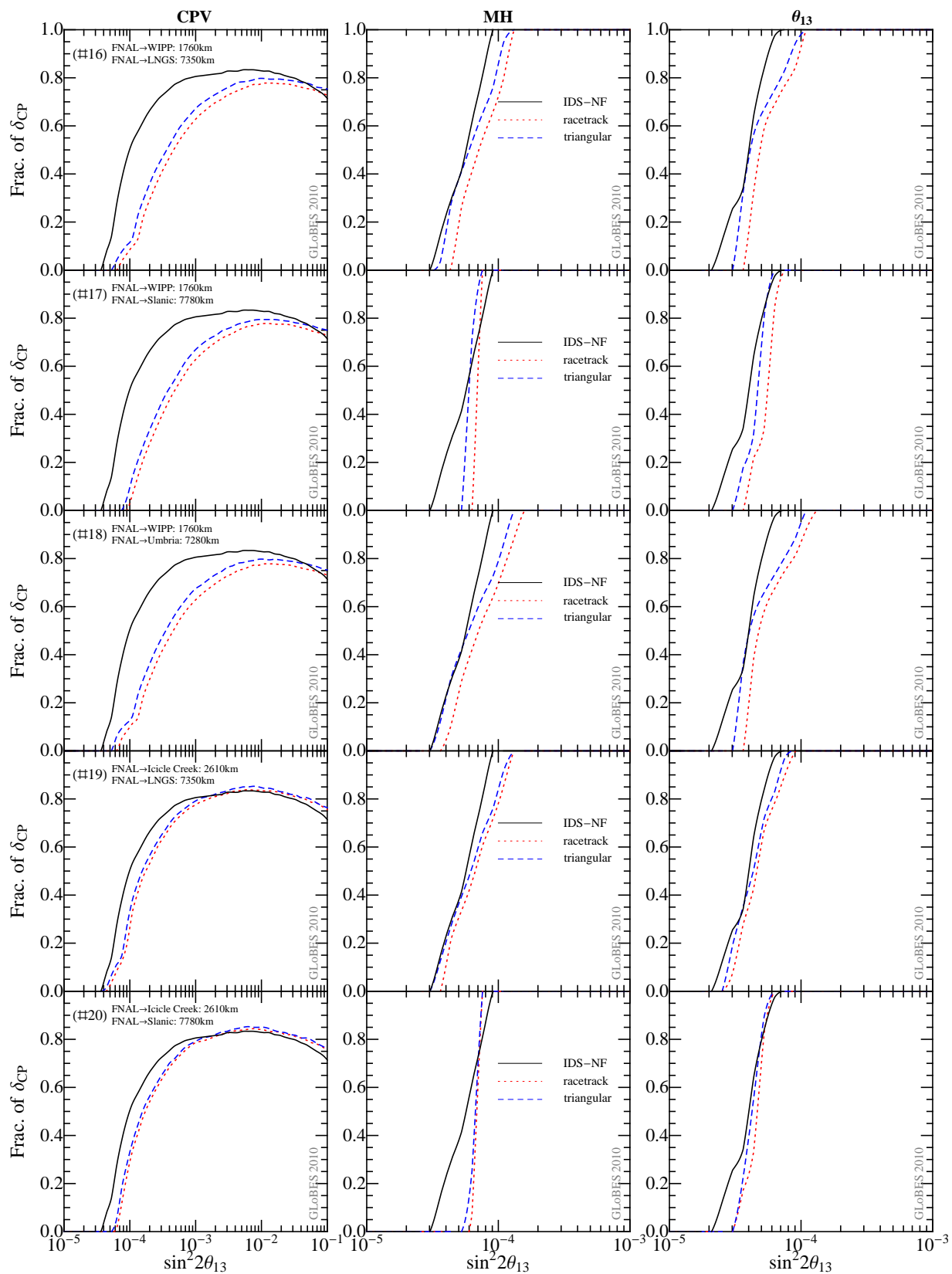


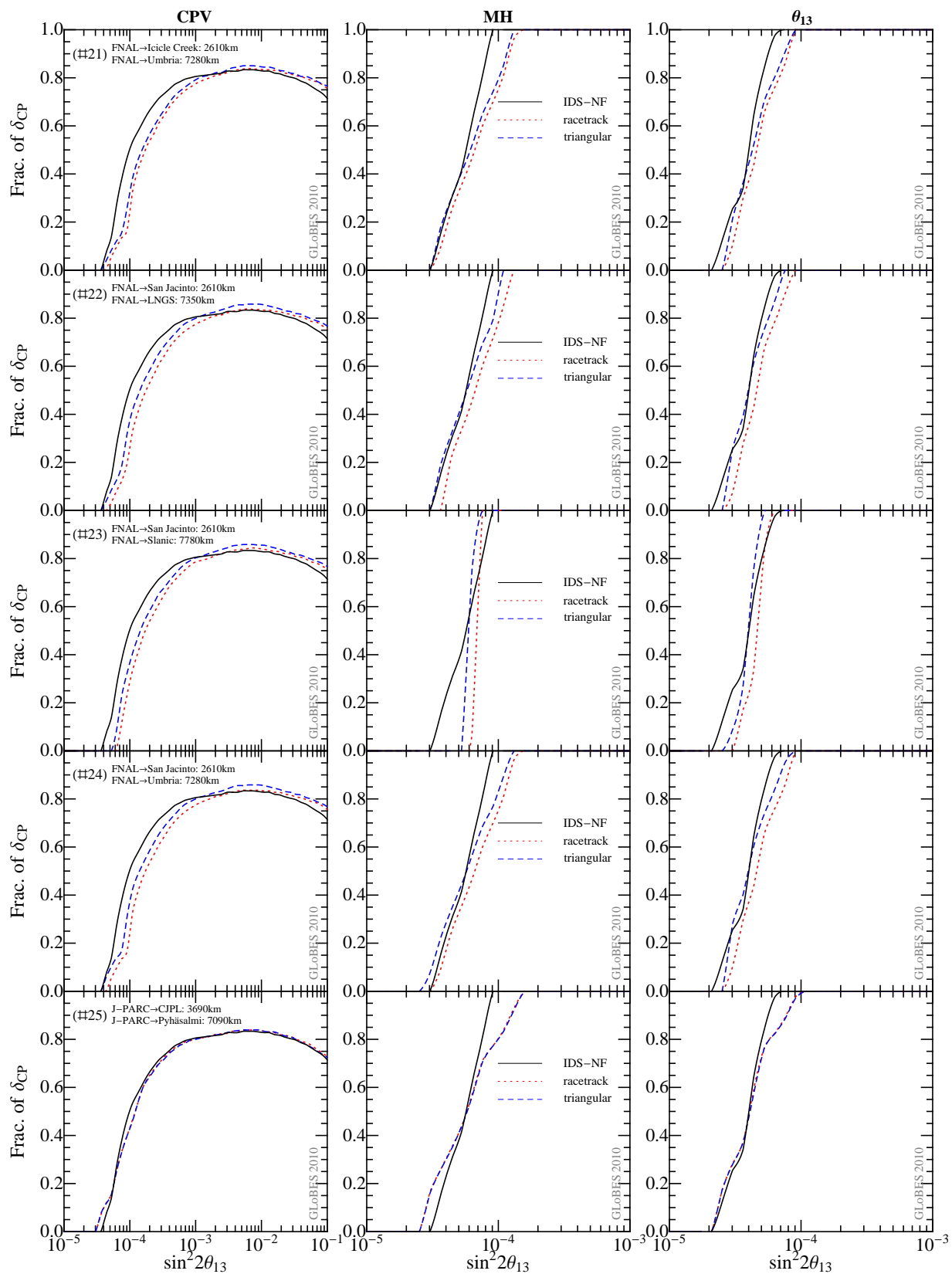


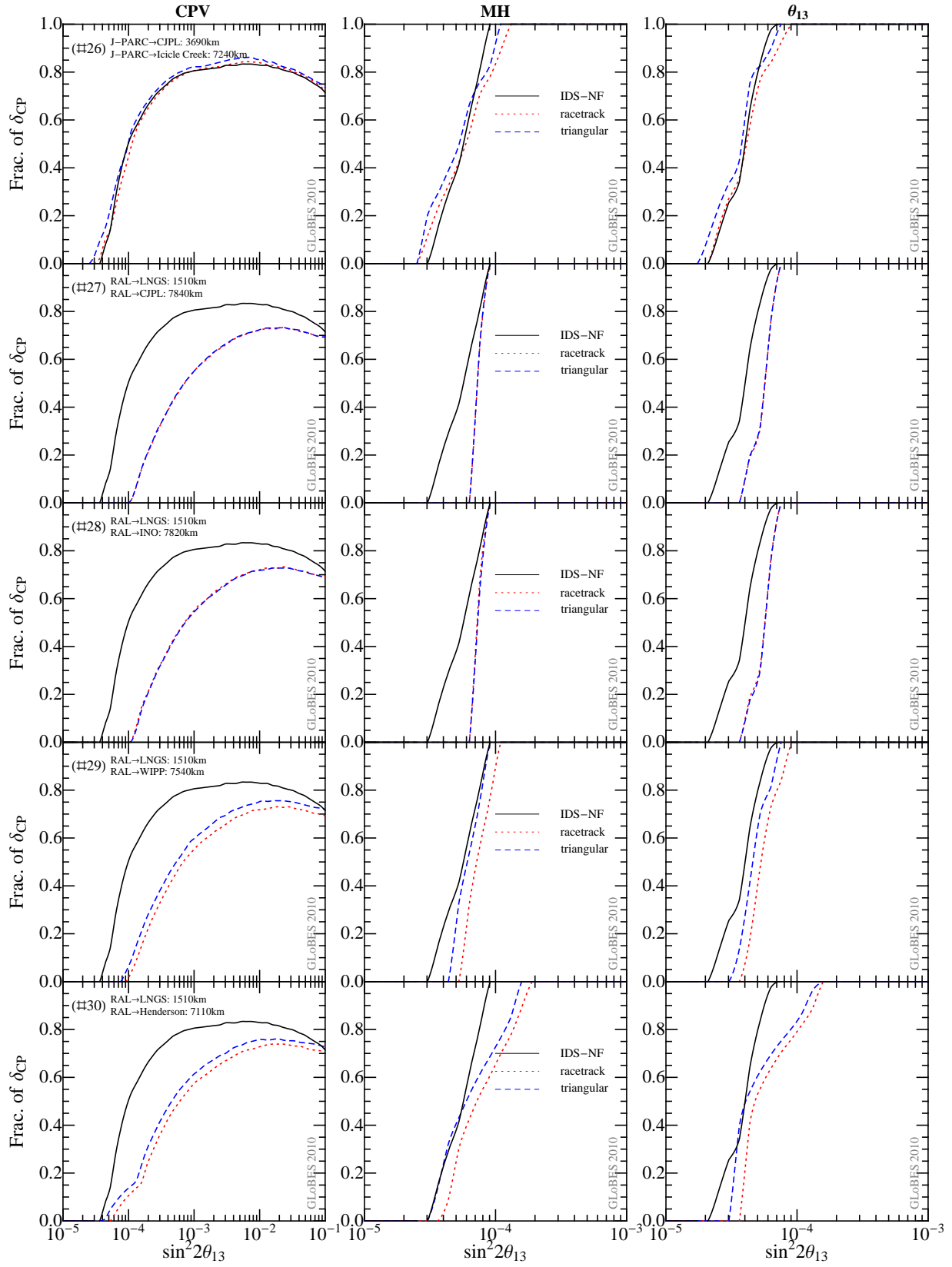
**Figure 16:** Discovery reach for CPV, MH, and  $\theta_{13}$  for the combinations listed in Table 3. Dotted (red) curves: SF=1 (racetrack-shaped storage rings), dashed (blue) curves: SF from Table 3 (triangular ring), black curves: IDS-NF baseline combination. Two 50 kt detectors used,  $3\sigma$  CL.

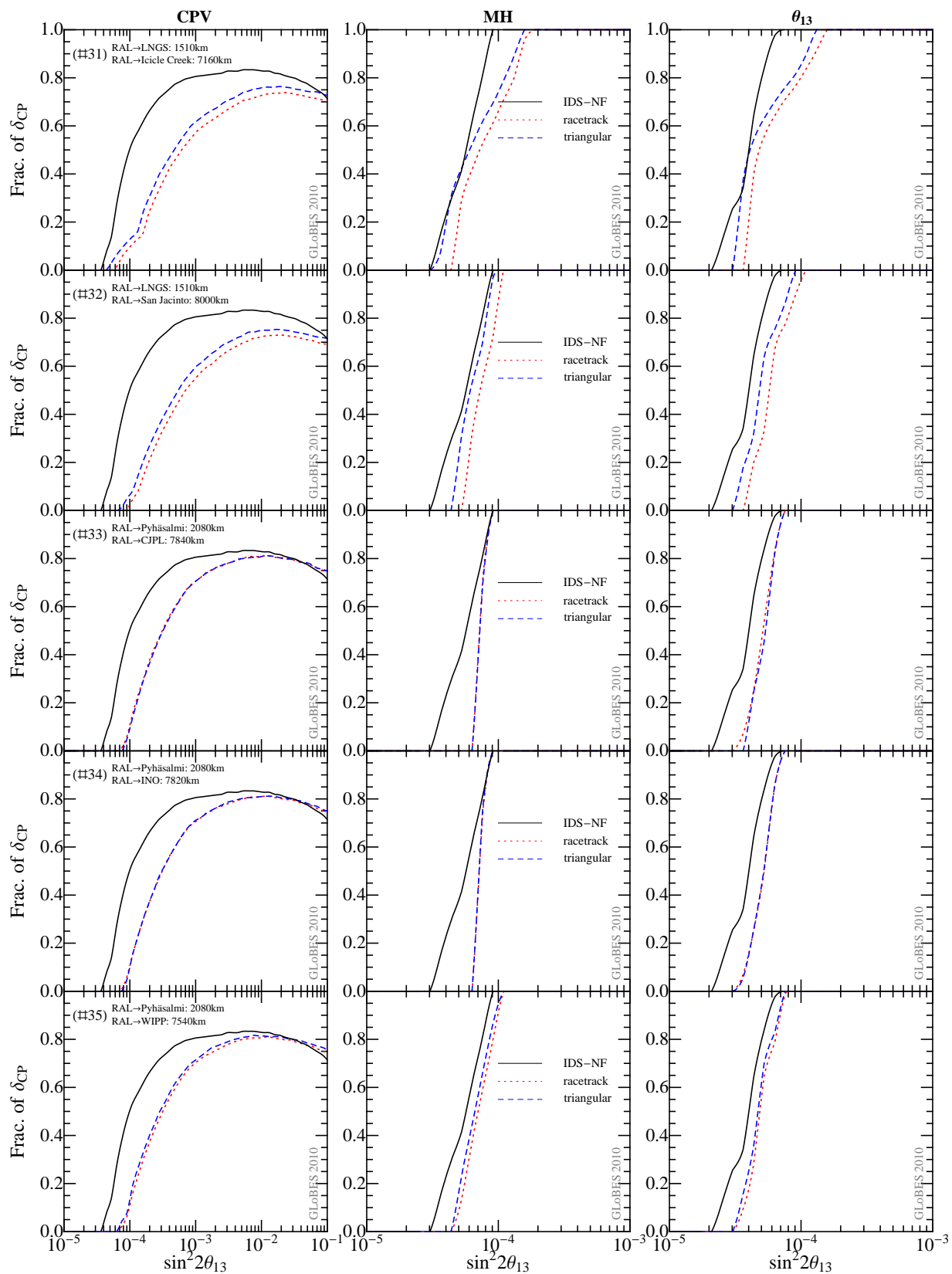


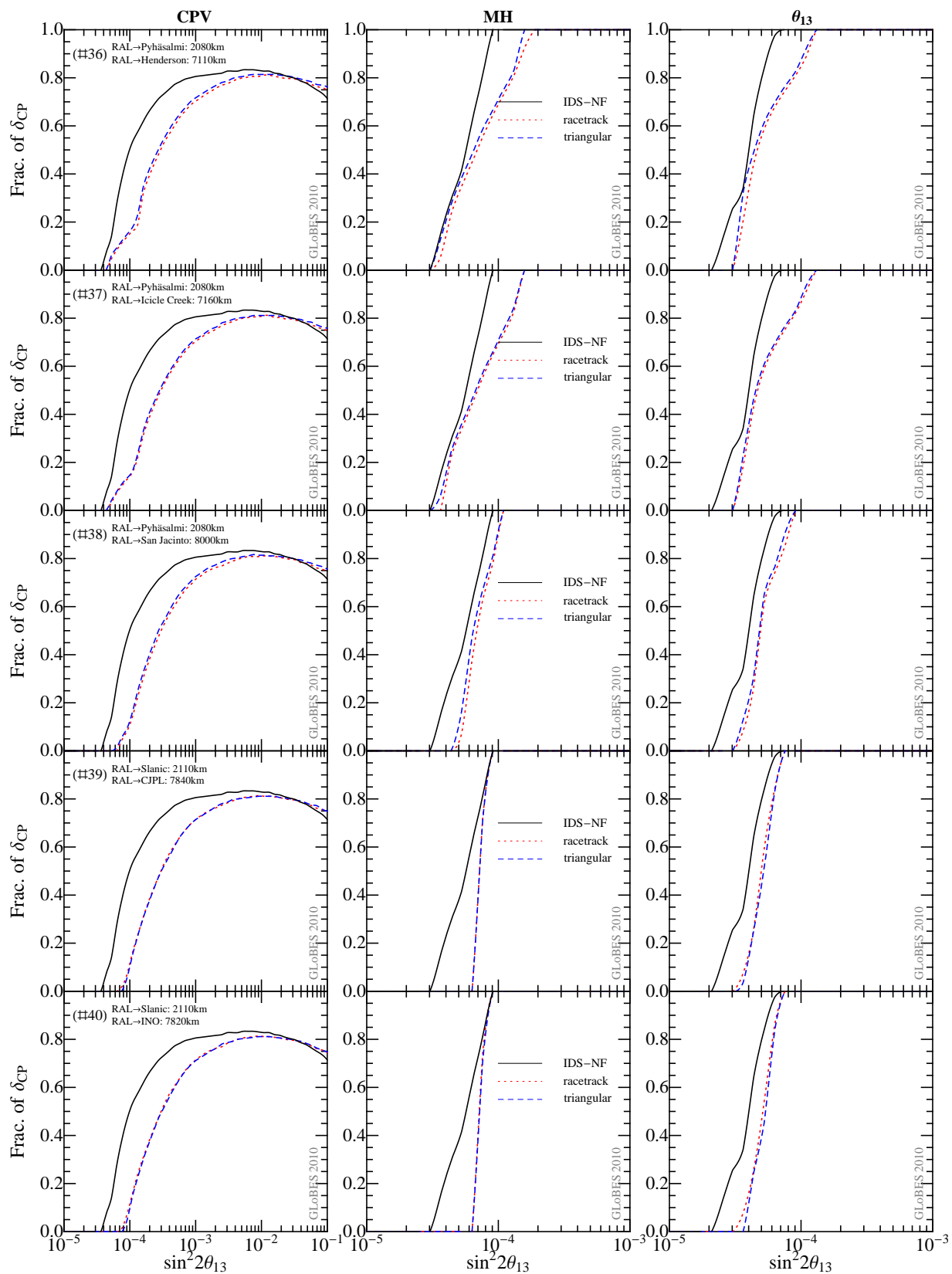




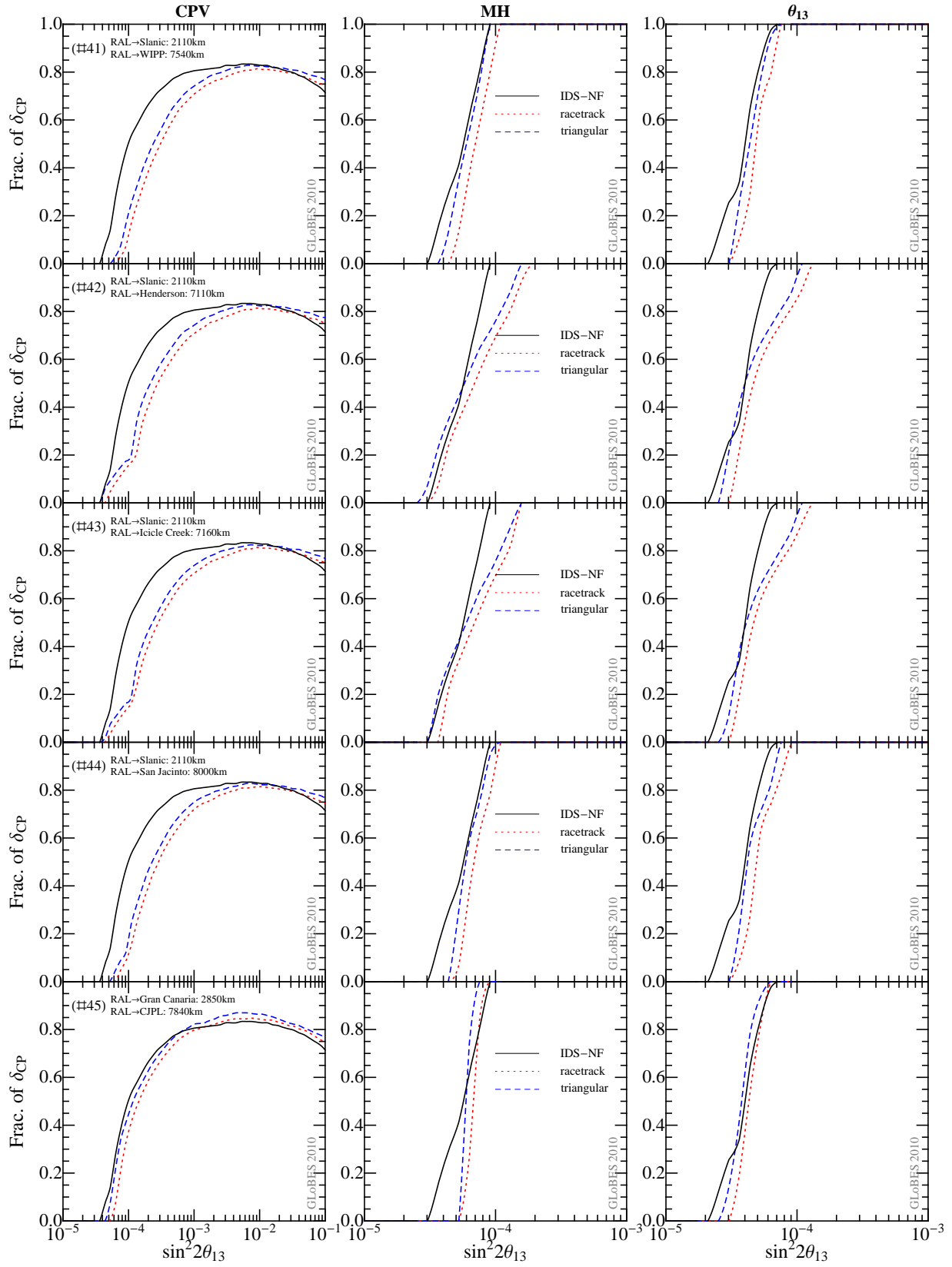


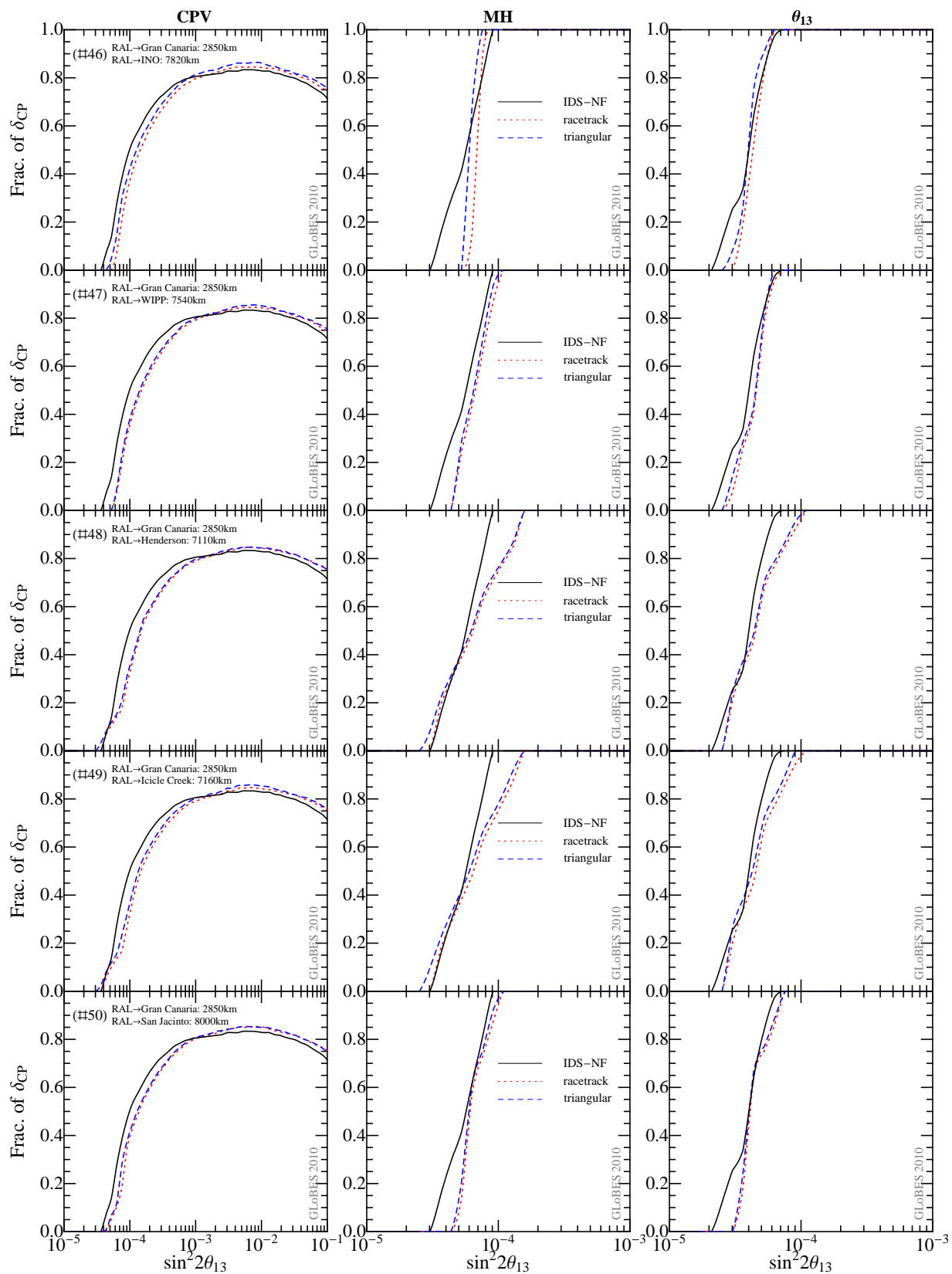












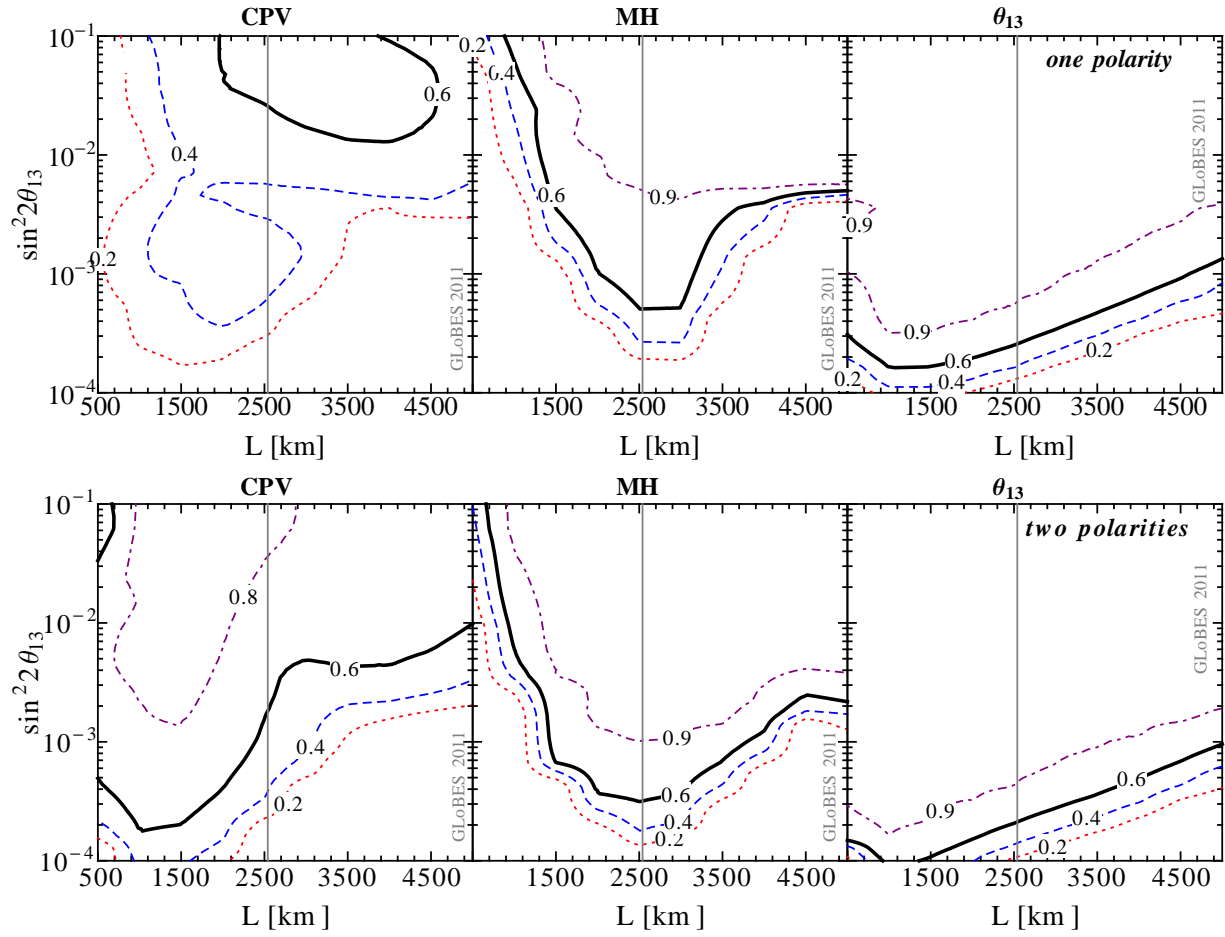


**Figure 17:** Discovery reach in  $\sin^2 2\theta_{13}$  as a function of baseline for CPV, MH, and  $\theta_{13}$  discovery and specific fractions of  $\delta_{CP}$  (contours) for a T ASD, see Ref. [48] for details. The upper row is for one polarity ( $\mu^+$  stored), the lower for two polarities. The results are shown at  $3\sigma$  CL with true normal hierarchy.

In Fig. 16 (see also following pages), we show the performances of the discussed combinations (#1 to #50) from Table 3. In each case, we compare the performances with racetracks (SF=1, dotted curves), triangular-shaped geometry (SF from Table 3, dashed curves), and IDS combination (SF=1, solid curves). The main results of these figures are already discussed in Sec. 5. The data points for the individual curves can be obtained at Ref. [40].

## C Note on the “bi-magic” baseline

In Ref. [48], the effect that the dependence on  $\delta_{CP}$  at a particular baseline and energy disappears (“bi-magic baseline”,  $L \simeq 2540$  km) for a chosen mass hierarchy, has been studied for a low energy neutrino factory together with a magnetized totally active scintillator detector (T ASD), which has somewhat different characteristics than the detector in this

study (somewhat better efficiencies at low energies and a better energy resolution). See also Ref. [51] for the bi-magic baseline in the context of a superbeam, and Ref. [52] for its baseline optimization. We have reproduced the simulation in Ref. [48] using the same beam and detector parameters, and we have studied the baseline dependence, see, Fig. 17, for the CPV, MH, and  $\theta_{13}$  discovery reaches. In this figure, specific values for the fraction of  $\delta_{\text{CP}}$  (contours) have been chosen to show the effect of the bi-magic baseline.

Our main observations from Fig. 17 with respect to Ref. [48] can be summarized as follows:

1. The optimal baseline choice depends on the performance indicator, the bi-magic baseline is mostly preferred for the MH. Measuring CPV would clearly lead to a different baseline optimization.
2. There is clear preference for using both muon polarities, which will lead to a much better absolute sensitivity.
3. There is no particular preference for exactly this baseline value, for none of the performance indicators, in the sense of the “magic baseline” [11] where a clear, narrow dip can be seen in the numerical study (see Figs. 3 and 6 in Ref. [18]). In addition, the “bi-magic effect” cannot be clearly attributed to the particular suggested energy windows. For example, if one masks the bins around the bi-magic energies (0.3 GeV windows around 1.9 and 3.3 GeV), the sensitivity is hardly affected.

We have tested that our observations do not rely on the true hierarchy, or the energy resolution of the detector.

In conclusion, the baseline of 2540 km is a good choice for the T ASD if one wants to measure the MH as primary performance indicator for as small as possible values of  $\sin^2 2\theta_{13}$ . There is, however, no preference of this exact baseline value, instead a relatively wide baseline window is allowed. In addition, if CPV is considered as most important, a different baseline optimization will be clearly preferred.

Finally, note that the logic of our paper is different: we have re-established the one baseline option of the low energy Neutrino Factory for  $\sin^2 2\theta_{13} \gtrsim 0.01$ . In this case, the mass hierarchy can be measured for all values of  $\delta_{\text{CP}}$  for  $L \gtrsim 1500$  km for the considered T ASD (in the most pessimistic case  $\sin^2 2\theta_{13} = 0.01$ ). This means that the baseline optimization will be driven by the CPV measurement under the boundary condition of a minimal baseline for the mass hierarchy, which is illustrated in Figs. 1 and 3 of Ref. [37]. From Fig. 17 (lower left panel), we can read off that for  $\sin^2 2\theta_{13} = 0.01$ , the smallest considered value for the LENF, the optimal baseline for both MH and CPV is then  $1500 \text{ km} \lesssim L \lesssim 2100 \text{ km}$  (requiring a fraction of  $\delta_{\text{CP}}$  of 80% for CPV and 100% for MH), which is roughly consistent to the MIND detector, see Fig. 5 upper right panel. On the other hand, for  $\sin^2 2\theta_{13} \lesssim 0.01$  ( $\theta_{13}$  not discovered by the next generation of experiments), a two baseline HENF will be the optimal choice, and the MH discovery will be driven by the very long baseline.

## References

- [1] M. C. Gonzalez-Garcia and M. Maltoni, Phys. Rept. **460**, 1 (2008), 0704.1800.
- [2] M. C. Gonzalez-Garcia, M. Maltoni, and J. Salvado, JHEP **04**, 056 (2010), 1001.4524.
- [3] G. L. Fogli, E. Lisi, A. Marrone, A. Palazzo, and A. M. Rotunno, Phys. Rev. Lett. **101**, 141801 (2008), 0806.2649.
- [4] S. Geer, Phys. Rev. **D57**, 6989 (1998), hep-ph/9712290.
- [5] *International design study of the neutrino factory*, <http://www.ids-nf.org>.
- [6] M. Apollonio *et al.* (2002), hep-ph/0210192.
- [7] C. Albright *et al.* (Neutrino Factory/Muon Collider) (2004), physics/0411123.
- [8] A. Bandyopadhyay *et al.* (ISS Physics Working Group) (2007), arXiv:0710.4947[hep-ph].
- [9] T. Abe *et al.* (ISS Detector Working Group), JINST **4**, T05001 (2009), 0712.4129.
- [10] J. S. Berg *et al.* (ISS Accelerator Working Group) (2008), 0802.4023.
- [11] P. Huber and W. Winter, Phys. Rev. **D68**, 037301 (2003), hep-ph/0301257.
- [12] V. Barger, S. Geer, and K. Whisnant, Phys. Rev. **D61**, 053004 (2000), \hfill\hep-ph/9906487.
- [13] A. Cervera *et al.*, Nucl. Phys. **B579**, 17 (2000), hep-ph/0002108.
- [14] J. Burguet-Castell, M. B. Gavela, J. J. Gomez-Cadenas, P. Hernandez, and O. Mena, Nucl. Phys. **B608**, 301 (2001), hep-ph/0103258.
- [15] M. Freund, P. Huber, and M. Lindner, Nucl. Phys. **B615**, 331 (2001), hep-ph/0105071.
- [16] A. Donini, E. Fernandez-Martinez, D. Meloni, and S. Rigolin, Nucl. Phys. **B743**, 41 (2006), hep-ph/0512038.
- [17] P. Huber, M. Lindner, M. Rolinec, and W. Winter, Phys. Rev. **D74**, 073003 (2006), hep-ph/0606119.
- [18] R. Gandhi and W. Winter, Phys. Rev. **D75**, 053002 (2007), hep-ph/0612158.
- [19] J. Kopp, T. Ota, and W. Winter, Phys. Rev. **D78**, 053007 (2008), 0804.2261.
- [20] N. C. Ribeiro, H. Minakata, H. Nunokawa, S. Uchinami, and R. Zukanovich-Funchal, JHEP **12**, 002 (2007), 0709.1980.
- [21] J. Tang and W. Winter, Phys. Rev. **D80**, 053001 (2009), arXiv:0903.3039.
- [22] P. Huber, M. Lindner, and W. Winter, Nucl. Phys. **B645**, 3 (2002), hep-ph/0204352.

- [23] A. Cervera, A. Laing, J. Martin-Albo, and F. J. P. Soler (2010), 1004.0358.
- [24] A. Laing, *Optimization of Detectors for the Golden Channel at a Neutrino Factory*, Ph.D. thesis, Glasgow university (2010).
- [25] *India-based neutrino observatory*, <http://www.ino.tifr.res.in/ino/>.
- [26] D. Indumathi and N. Sinha, Phys.Rev. **D80**, 113012 (2009), arXiv:0910.2020.
- [27] A. Donini, J. J. Gomez Cadenas, and D. Meloni (2010), 1005.2275.
- [28] R. Acquafredda *et al.* (OPERA), New J. Phys. **8**, 303 (2006), hep-ex/0611023.
- [29] A. Donini, D. Meloni, and P. Migliozzi, Nucl. Phys. **B646**, 321 (2002), hep-ph/0206034.
- [30] D. Autiero *et al.*, Eur. Phys. J. **C33**, 243 (2004), hep-ph/0305185.
- [31] A. Donini, K.-i. Fuki, J. Lopez-Pavon, D. Meloni, and O. Yasuda, JHEP **08**, 041 (2009), 0812.3703.
- [32] S. Geer, O. Mena, and S. Pascoli, Phys. Rev. **D75**, 093001 (2007), hep-ph/0701258.
- [33] A. D. Bross, M. Ellis, S. Geer, O. Mena, and S. Pascoli, Phys. Rev. **D77**, 093012 (2008), 0709.3889.
- [34] P. Huber and W. Winter, Phys. Lett. **B655**, 251 (2007), 0706.2862.
- [35] A. Bross *et al.*, Phys. Rev. **D81**, 073010 (2010), 0911.3776.
- [36] E. Fernandez Martinez, T. Li, S. Pascoli, and O. Mena, Phys. Rev. **D81**, 073010 (2010).
- [37] J. Tang and W. Winter, Phys. Rev. **D81**, 033005 (2010), 0911.5052.
- [38] P. Cushman (2006), talk given at the Topical Workshop on Low Radioactivity Techniques, October 1-4, 2006, Aussois, France, <http://lrt2006.in2p3.fr/talks/LRT06-Pcushman.pdf>.
- [39] *Laguna - large apparatus studying grand unification and neutrino astrophysics*, <http://www.laguna-science.eu/>.
- [40] *Individual site performance data file web page*, <http://www.phys.vt.edu/~pahuber/neutrino-factory-sites.html>.
- [41] P. Huber, M. Lindner, and W. Winter, Comput. Phys. Commun. **167**, 195 (2005), <http://www.mpi-hd.mpg.de/lin/globes/>, hep-ph/0407333.
- [42] P. Huber, J. Kopp, M. Lindner, M. Rolinec, and W. Winter, Comput. Phys. Commun. **177**, 432 (2007), hep-ph/0701187.
- [43] R. J. Geller and T. Hara, Phys. Rev. Lett. **49**, 98 (2001), hep-ph/0111342.

- [44] T. Ohlsson and W. Winter, Phys. Rev. **D68**, 073007 (2003), [hep-ph/0307178](#).
- [45] M. Freund, Phys. Rev. **D64**, 053003 (2001), [hep-ph/0103300](#).
- [46] E. K. Akhmedov, R. Johansson, M. Lindner, T. Ohlsson, and T. Schwetz, JHEP **04**, 078 (2004), [hep-ph/0402175](#).
- [47] P. Huber, M. Lindner, and W. Winter, Nucl. Phys. **B654**, 3 (2003), [hep-ph/0211300](#).
- [48] A. Dighe, S. Goswami, and S. Ray, Phys. Rev. Lett. **105**, 261802 (2010), [1009.1093](#).
- [49] *Google maps*, <http://maps.google.com/>.
- [50] P. Huber, M. Lindner, T. Schwetz, and W. Winter, JHEP **0911**, 044 (2009), [0907.1896](#).
- [51] S. K. Raut, R. S. Singh, and S. Sankar (2009), [0908.3741](#).
- [52] V. Barger, M. Dierckxsens, M. Diwan, P. Huber, C. Lewis, *et al.*, Phys.Rev. **D74**, 073004 (2006), [hep-ph/0607177](#).